ChemComm

FEATURE ARTICLE

View Article Online
View Journal

Cite this: DOI: 10.1039/d5cc07349a

Copper nanoclusters with atomic precision as catalyst for organic reactions

Rupa Sarma, Sourav Mandal, Dipanwita Rout, Mandira Ghosh, Tokuhisa Kawawaki, Sourav Biswas * and Yuichi Negishi *

Atomically precise copper nanoclusters (Cu NCs) have emerged as a distinctive class of catalysts that bridge molecular complexes and conventional nanoparticles. Their well-defined nuclearity, discrete electronic structures, and tunable ligand environments enable direct structure–activity correlations that are inaccessible with traditional Cu catalysts. This review summarizes recent advances in the use of atomically precise Cu NCs as organocatalysts for a broad range of organic transformations, including cycloadditions, C–C and C–N coupling reactions, hydroboration, hydrogenation, oxidation, protosilylation, sulfonylation, and multicomponent reactions. Emphasis is placed on how subtle structural features—such as nuclearity, hydride content, ligand dynamics, surface defects, mixed-valence states, and exposed metal sites—govern catalytic activity, selectivity, and reaction mechanisms. Representative examples illustrate that Cu NCs can operate *via* radical or polar pathways, act as intrinsic photo- and redox catalysts, and exhibit single-site behavior in both homogeneous and heterogeneous systems. Overall, this review highlights key structure–activity relationships and outlines emerging design principles and future opportunities for developing efficient, sustainable, and earth-abundant Cu-based catalysts.

Received 26th December 2025,
Accepted 31st March 2026

DOI: 10.1039/d5cc07349a

rsc.li/chemcomm

1. Introduction

Research on atomically precise metal nanoclusters (NCs) originated from their extraordinary photophysical properties, which arise from size-dependent quantum confinement effects and discrete electronic energy levels.[1–5] Unlike conventional metal nanoparticles, NCs possess quantized electronic orbitals and well-defined molecular-like electronic structures, enabling strong correlations between their atomic arrangement, electronic configuration, and optical response.[6–13] In parallel, their fascinating structural architectures—ranging from core–shell motifs to ligand-protected metal frameworks—have stimulated extensive efforts toward understanding structure–property relationships and expanding the library of atomically precise NCs.[14–17]

In the early stages of NC research, a major challenge was their limited stability in solution, which severely restricted

Institute of Multidisciplinary Research for Advanced Materials, Tohoku University, Katahira 2-1-1, Aoba-ku, Sendai 980-8577, Japan.
E-mail: Sourav.biswas210@gmail.com, yuichi.negishi.a8@tohoku.ac.jp

Rupa Sarma

Rupa Sarma is a PhD researcher in Prof. Negishi's group at Tohoku University, Japan. She obtained her Master's degree in Chemistry from National Institute of Technology Durgapur, India (2022). Her research focuses on the synthesis of atomically precise copper nanoclusters, analysing crystal structures, detailed investigation of their photophysical properties, and exploration of their catalytic and functional applications.

Sourav Mandal

Sourav Mandal is a PhD student in Prof. Negishi's group at Tohoku University, Japan. He received his Master's degree in Chemistry from Banaras Hindu University, India, in 2023. His current research focuses on the synthesis of diverse copper nanoclusters for electrocatalytic nitrate reduction toward renewable energy applications.

detailed characterization and hindered exploration of their functional applications.[18,19] This instability was primarily associated with weak metal–ligand interactions and susceptibility to aggregation or oxidation.[20,21] However, rapid advances in synthetic methodologies and surface protection strategies have largely overcome these limitations.[15,22–27] The development of robust ligand shells—such as thiolates, phosphines, N-heterocyclic carbenes, carborane and alkynyl ligands—has enabled strong metal–ligand interactions, significantly enhancing the chemical and thermal stability of NCs.[28–33] These advances further facilitated the transition from noble-metal-based NCs to those composed of first-row transition metals, thereby broadening compositional diversity while maintaining structural precision and stability. The availability of stable and well-defined NCs marked a pivotal shift in research focus from purely photophysical investigations toward functional applications. In particular, the atomically precise structures, high surface atom exposure, and tunable electronic states of NCs make them highly attractive candidates for catalysis.[4,34–37] Unlike traditional heterogeneous catalysts, which often suffer from ill-defined active sites and limited structure–activity correlations, NCs offer an unparalleled platform for correlating catalytic performance with precise atomic structures and electronic configurations. Consequently, metal NCs have emerged as a new class of catalysts capable of overcoming many intrinsic limitations associated with conventional transition-metal catalysts, such as poor selectivity, low atom efficiency, and limited mechanistic insight.[38–42]

As the scope of NC research expanded beyond noble metals, copper (Cu) NCs rapidly gained attention due to earth abundance of elemental Cu, low cost, multiple accessible oxidation states, and favorable redox potentials.[43–52] These intrinsic properties, combined with atomic precision and ligand-induced electronic modulation, render Cu NCs particularly promising for catalytic applications. As a result, a rapidly growing body of literature now demonstrates the extensive use of Cu NCs as catalysts in a wide range of chemical transformations. These applications span diverse areas, including organic transformations, electrocatalytic and photocatalytic reduction reactions, and the conversion of both organic and inorganic substrates.[53–59] Notably, the most pronounced diversity and performance enhancements have been observed in organic transformation reactions, where the catalytic activity, selectivity, and reaction pathways are highly sensitive to the

Dipanwita Rout

Dipanwita Rout is a PhD student in Prof. Negishi's research group at Tohoku University, Japan. She obtained her Master's degree in Chemistry from the National Institute of Technology, Durgapur (2022). Subsequently, she worked as a Project Associate-I at CSIR-CSMCRI Bhavnagar (2024). Her current research focuses on the synthesis of copper nanoclusters and their catalytic applications.

Mandira Ghosh

Mandira Ghosh is a PhD student in in Prof. Negishi's group at Tohoku University, Japan. She received her Master's in Chemistry from National Institute of Technology Durgapur (2022). Afterward she joined at Vellore Institute of Technology, Chennai (2023) as Junior Research Fellow. Her current research focus on the synthesis of different Cu nanocluster for the electrocatalytic CO_2 reduction reaction.

Sourav Biswas

Sourav Biswas is an Assistant Professor of the Institute of Multidisciplinary Research for Advanced Materials at Tohoku University, Japan. He obtained his PhD in Chemistry from the National Institute of Technology Durgapur, India (2020). He did his postdoctoral research in Indian Institute of Science Education and research Thiruvananthapuram, India and Tokyo University of Science Japan. His recent research interests focus on the synthesis and investigation of potential applications for nanoclusters.

Yuichi Negishi

Yuichi Negishi is a Professor of the Institute of Multidisciplinary Research for Advanced Materials at Tohoku University. He received his PhD degree in Chemistry (2001) from Keio University. Prior to joining Tohoku University in 2024, he was employed as a Professor at Tokyo University of Science since 2008 and before that worked as an Assistant Professor at Keio University and the Institute for Molecular Science. His research interests include the structural and functional exploration of atomically precise metal NCs, metal NC-assembled materials, and covalent organic frameworks.

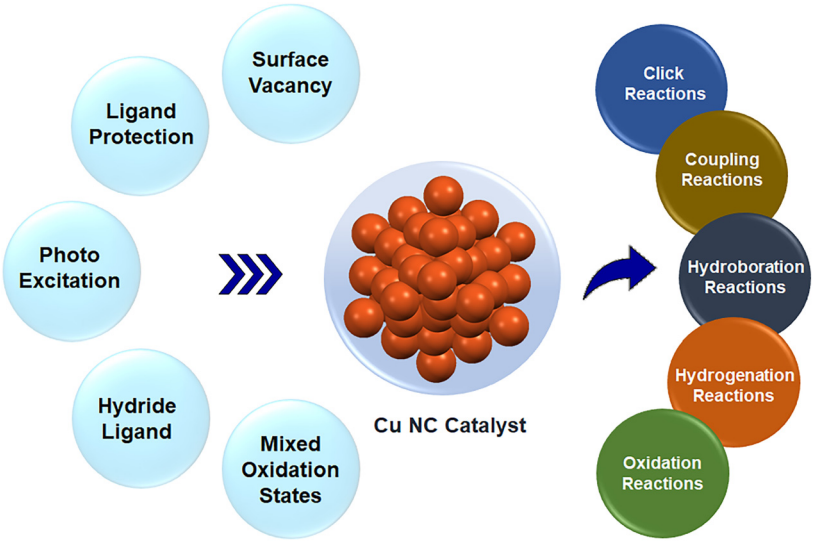

Fig. 1 Schematic representation of utilization of diverse Cu NCs in diverse organocatalytic reactions.

structural architecture of the Cu NCs (Fig. 1).[60] Importantly, organic catalytic transformations play a pivotal role in modern synthetic chemistry by enabling the efficient construction and functionalization of molecular architectures through controlled substrate activation, electron-transfer processes, and radical or polar reaction pathways. Accordingly, catalysts with atomically well-defined structures are particularly valuable because they allow direct correlation between electronic structure, active-site geometry, and catalytic reactivity in complex organic transformation. Parameters such as nuclearity, ligand environment, surface defects, and oxidation state distribution play critical roles in governing catalytic behavior. Despite several earlier review efforts summarizing aspects of Cu-based NC catalysis, the exceptionally rapid growth of this field necessitates an updated and comprehensive assessment that incorporates recent discoveries, particularly those emphasizing structure–activity relationships.[60,61] However, although a range of analytical techniques—including single-crystal X-ray diffraction (SCXRD), electrospray ionization mass spectrometry (ESI-MS), Extended X-ray absorption fine structure (EXAFS), and high-resolution transmission electron microscopy (HR-TEM)—are available for determining the structures of NCs, SCXRD remains the most comprehensive and reliable method (Scheme 1). This is because it provides precise atomic-level insights into both their geometric and electronic structures. Therefore, in this review, we primarily focus on the catalytic reactivity of nanoclusters whose structural architectures have been unambiguously resolved by SCXRD, enabling a clear correlation between their well-defined structures and observed catalytic properties.

In this review, we systematically summarize recent progress in the application of Cu NCs in organic transformation reactions, with a particular emphasis on elucidating the roles of atomic precision, structural architecture, and electronic structure in determining catalytic performance (Fig. 1). Comparisons with conventional catalytic systems are provided to highlight the unique advantages of Cu NCs. Finally, we discuss emerging trends and future directions in this rapidly evolving area, focusing on how strategic structural evolution and rational ligand design are shaping the next generation of Cu–NC-based catalysts.

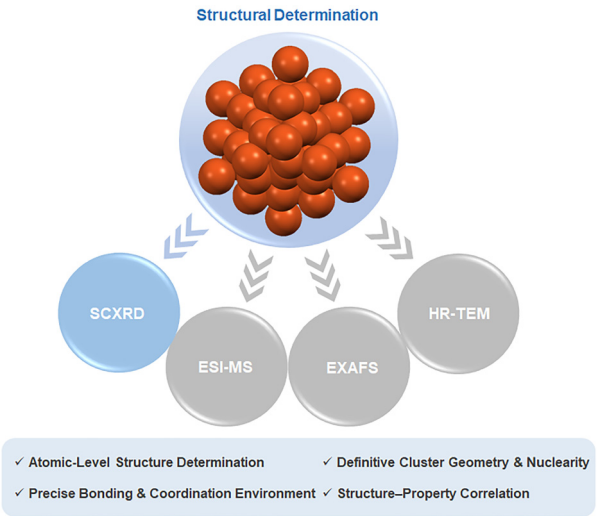

Scheme 1 Analytical techniques are available for the structural determination of NCs.

2. Utilization of Cu NCs in organic transformation reactions

The development of Cu NCs can be traced back to the early synthesis of copper-hydride (CuH) NCs, which represented one of the first attempts to isolate atomically precise Cu-based species with cluster-like electronic structures.[62–67] These CuH NCs attracted significant interest due to their unique electronic characteristics and their conceptual similarity to molecular metal hydride complexes.[64] However, the intrinsic instability

of CuH NCs—stemming from weak metal–H bonding, high susceptibility to oxidation, and structural lability in solution—severely limited their long-term stability and practical applicability. As a result, systematic studies on their catalytic behavior, mechanistic pathways, and recyclability remained challenging. The introduction of surface protection strategies marked a turning point in Cu NC research.[68–70] The incorporation of strongly coordinating ligands significantly enhanced the stability without compromising atomic precision. These surface-protecting units not only prevented aggregation and oxidation of the Cu core but also played an active role in modulating the electronic structure and surface reactivity of the NCs. Consequently, ligand-protected Cu NCs emerged as a stable and versatile platform for both fundamental investigations and applied catalysis.[53,71]

It is noteworthy that CuH complexes and related C–H–Cu species are well established as efficient catalysts for a variety of organic transformations, including hydrogenation, hydroamination, hydrosilylation, and C–H functionalization reactions.[72–75] Nevertheless, when translated to the regime, the weak stability of hydride-containing Cu NCs restricts their isolation and hinders direct evaluation of their catalytic potential under practical reaction conditions. This limitation underscores the importance of ligand-stabilized Cu NCs, where the hydride motif may be transient or generated *in situ*, while the overall cluster framework remains structurally intact. The availability of a diverse library of stable Cu NCs has therefore significantly broadened the scope of Cu-based NC catalysis.[68] These well-defined NCs enable systematic exploration of structure–activity relationships, revealing how parameters such as nuclearity, ligand environment, surface defects, and oxidation-state distribution influence catalytic performance. As a result, Cu NCs have been successfully employed in a wide range of organic transformation reactions, often exhibiting superior selectivity, enhanced atom efficiency, and unique reaction pathways compared to conventional copper catalysts and nanoparticles. In the following sections, we comprehensively summarize representative organic transformation reactions catalyzed by Cu NCs, with particular emphasis on the role of cluster stability and structural architecture in governing catalytic activity and selectivity.

2.1. Click reaction

Cook *et al.* reported a mixed-valent $[Cu_{20}(CCPh)_{12}(OAc)_6]$ (Cu_{20}) (CCPh = phenyl acetylide; OAc = acetate) NC, where a tetrahedral $[Cu_4]^{2+}$ kernel is encapsulated within a $[Cu_{16}(CCPh)_{12}(OAc)_6]^{2-}$ shell.[76] This structure represents the first example of a Cu-only superatom featuring a tetrahedral core, hosting a two-electron superatomic configuration. Cu_{20} efficiently catalyzed the [3 + 2] cycloaddition between benzyl azide ($PhCH_2N_3$) and a broad range of terminal alkynes—including phenylacetylene ($HC\equiv CPh$), ethyl propiolate ($HC\equiv CCO_2Et$), and *tert*-butyl acetylene ($HC\equiv C^tBu$)—producing the corresponding 1,2,3-triazoles in excellent yields (Fig. 2). The well-defined Cu_{20} framework provides accessible Cu(I) sites that can promote azide–alkyne cycloaddition without requiring catalyst pretreatment, while the ligand-protected structure prevents aggregation during catalysis. Remarkably, high activity was maintained even at catalyst loadings as low as 0.05 mol%. An intriguing observation was the formation of 1-benzyl-4-phenyl-1*H*-1,2,3-triazole when alkynes other than $HC\equiv CPh$ were employed. This indicated direct involvement of the phenylacetylide ligands in the catalytic cycle. The authors proposed a mechanism in which $PhCH_2N_3$ first reacts with a ligand-derived phenyl acetylide to form a Cu-bound triazolate intermediate. Subsequent protonolysis by an external alkyne releases the triazole product and regenerates the copper-acetylide site, sustaining the catalytic turnover. The study further distinguished the performance of Cu_{20} NC in homogeneous *versus* heterogeneous environments. For the heterogeneous variant, the Cu_{20} NC was grafted onto dry, partially dehydroxylated silica, with immobilization accompanied by the loss of one phenylacetylide ligand per cluster, generating a Cu–O–Si linkage. While the homogeneous catalyst exhibited signs of structural degradation during reaction, the silica-supported cluster retained both its structural fidelity and catalytic efficiency across multiple cycles. No detectable Cu leaching was observed, confirming that catalysis originated from the intact immobilized NC rather than from dissolved Cu^+ species. Overall, this work establishes Cu NCs as a robust and versatile catalyst that performs efficiently in both homogeneous and supported heterogeneous forms. It further shows that immobilization on a solid support preserves the structural integrity of atomically precise Cu NCs, enhancing their stability, preventing leaching, and enabling reusability—crucial features for next-generation copper-based catalysts.

Thus, the previous study established an important model for employing Cu NCs as heterogeneous catalysts. This concept subsequently influenced several related works, where Cu NCs were used heterogeneously even when water-soluble variants were available. In this context, Yang *et al.* reported such water-soluble variant, $[Cu_{30}(MBA)_{16}]$ (Cu_{30}) (MBA = 4-mercaptobenzoic acid) NC, and evaluated its catalytic performance in azide–alkyne cycloaddition under heterogeneous conditions by immobilizing it onto amine-functionalized TiO_2 nanoparticles (TiO_2–NH_2) (Fig. 2).[77] The supported catalyst exhibited a substantially higher yield (94%) than the unsupported cluster at room temperature. This improvement was attributed to enhanced dispersion of Cu_{30} NC on the support surface, which increased the number of accessible active sites and provided superior structural stability during repeated catalytic cycles. In particular, anchoring the nanocluster on TiO_2–NH_2 significantly enhances its structural stability and prevents aggregation, allowing the catalyst to be reused over multiple reaction cycles. X-ray photoelectron spectroscopy (XPS) analysis revealed that ~67% of the Cu centers were present as Cu(I), the oxidation state primarily responsible for high activity in click-type cycloadditions. Substrate-scope studies showed that the nature of alkyne substituents strongly affected reaction efficiency: electron-donating or sterically bulky groups led to reduced yields due to steric hindrance or lower alkyne reactivity, whereas smaller or electron-withdrawing substituents afforded higher conversions. Thus, the findings highlight the combined steric and electronic factors that govern the catalytic

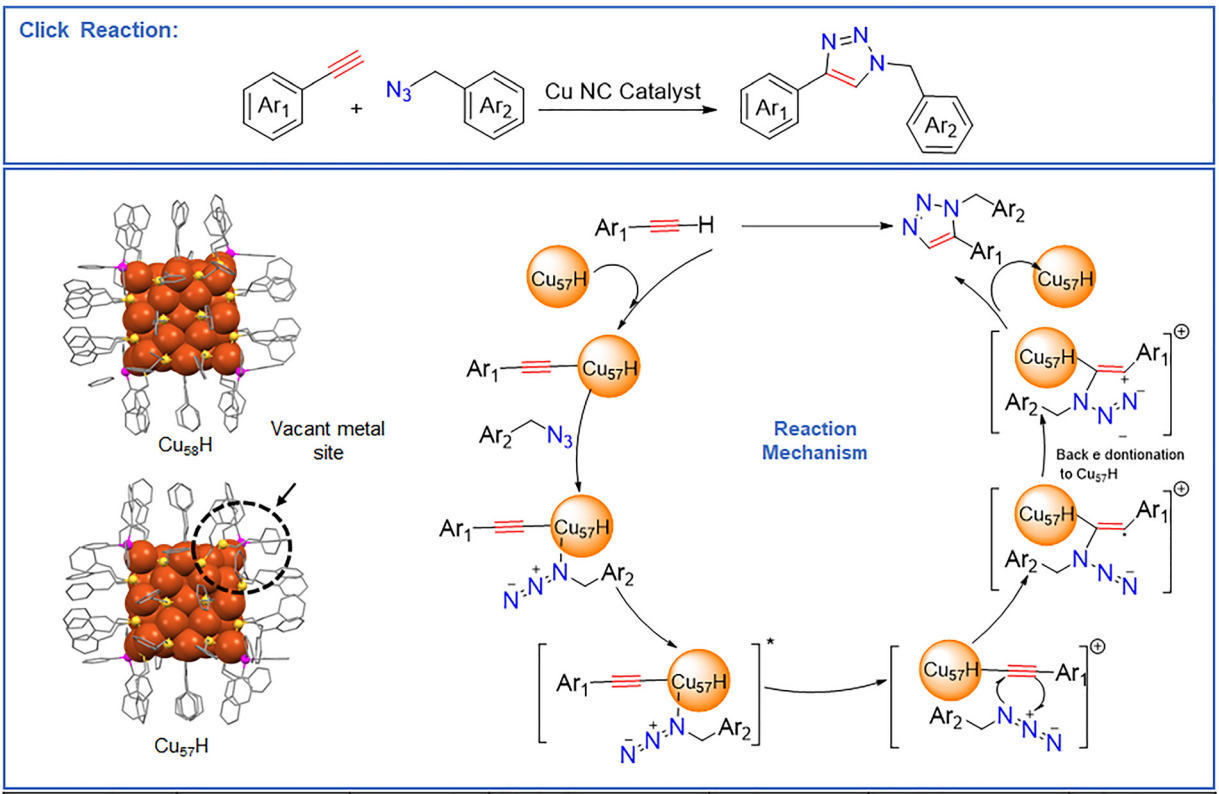

Catalyst	Loading (mol %)	Time (h)	Temperature (°C)	Solvent	Light	Yield (%)
Cu_{20} NC	1-2	2	25	CD_2Cl_2	No light	99
Cu_{22}-1 NC	1	1	30	CH_3CN	Visible light	90
Cu_{30} NC	0.5-1	24	RT	CH_3CN	No Light	94
$[Cu_8I_{14}]^{2-}$NC	1	10	RT	CH_3CN	Visible Light	90
$Cu_{57}H$ NC	0.025	1.5	30	CH_3CN	Blue LED	97
$Cu_{58}H$ NC	0.025	1.5	30	CH_3CN	Blue LED	77

Fig. 2 Representation of click reaction and utilization of diverse Cu NCs with diverse yields and the associated reaction mechanism by utilizing $Cu_{57}H$ NC.

performance of the Cu_{30} NC in promoting azide–alkyne cycloaddition.

The individual Cu NCs demonstrate significant potential for cycloaddition reactions; however, understanding how their precise structural architectures influence catalytic behaviour requires direct comparison of well-defined structural isomers. Such controlled studies become feasible when isomeric NCs are available. Zhou *et al.* reported the catalytic activity of two such structural isomers, Cu_{22}-1 and Cu_{22}-2, both formulated as $[Cu_{22}(SePh)_{10}(Se)_6[P(Ph\text{-}4F)_3]_8]$ (SePh = phenylselenide, P(Ph-4F)$_3$ = tris(4-fluorophenyl)phosphine) in cycloaddition reaction (Fig. 2).[78] Single-crystal X-ray diffraction (SCXRD) data revealed that each NC contains a similar $Cu_{16}Se_6$ core which is capped by $Cu(SeR)_3(P(Ph\text{-}4F)_3)$ surface motifs. The isomerism originates from different spatial arrangements of these capping motifs, which leads to distinct bonding environments and packing interactions through C–F···H–C and π···π interactions. These structural differences translate into measurable electronic and optical distinctions: Cu_{22}-1 exhibits a shoulder at 420 nm and a band gap of 2.60 eV, whereas Cu_{22}-2 shows a weaker absorption at 382 nm with a band gap of 2.73 eV. DFT (density functional theory) and TDDFT (time dependent density functional theory) analyses further corroborated subtle differences in orbital distributions and oscillator strengths. The two isomers displayed markedly different catalytic activities in the [3 + 2] azide–alkyne cycloaddition between $PhCH_2N_3$ and HC≡CPh. Under thermal conditions (50 °C, 0.06 mol% catalyst), Cu_{22}-1 delivered a 92% yield in 24 h, while Cu_{22}-2 achieved only 36%. The disparity was even more pronounced under 405 nm irradiation: Cu_{22}-1 reached 90% yield within 1 h, whereas Cu_{22}-2 afforded just 10%. The superior performance of Cu_{22}-1 arises from its more favourable surface-motif configuration and higher oscillator strength (0.01004 *vs.* 0.00405), which enhance light absorption and electron–hole pair generation, thereby boosting photocatalytic efficiency. Ultraviolet-visible (UV-vis) absorbance and powder X-ray diffraction (PXRD) analyses confirmed that

both NCs remained structurally intact after catalysis. Thus, this study demonstrates that even subtle variations in the structural architecture of Cu NCs can significantly alter their overall catalytic activity. Therefore, designing the appropriate geometry is crucial for maximizing the catalytic performance of NCs. However, several strategies reported in the literature show that structural activation of existing NCs can also enhance their catalytic activity, enabling otherwise inert clusters to function as efficient catalysts.

Xiao *et al.* reported a controlled synthetic approach to confine a dimeric $[Cu_8I_{14}]^{2-}$ NC in a supramolecule through host–guest interaction and identified its catalytic activity azide–alkyne cycloaddition (Fig. 2).[79] The confined supramolecular $[Cu_8I_{14}]^{2-}$ NC provides multiple accessible Cu(I) sites and promotes efficient charge separation under visible light irradiation, thereby enhancing photocatalytic performance. In benzylamine oxidation, it achieved up to 95% conversion and 76% yield under 455 nm irradiation and O_2, outperforming free CuI and the ligand alone. Although minor structural degradation was observed, the catalyst retained most of its activity over three cycles. In addition, this self-assembly also delivered up to 90% yield for the coupling of $HC{\equiv}CPh$ and $PhCH_2N_3$ under blue light within 10 hours. Electron-donating substituents enhanced yields, whereas electron-withdrawing groups decreased them (56–77%). 2,2,6,6-Tetramethylpiperidine-1-oxyl (TEMPO) quenching significantly suppressed reactivity, confirming a photoinduced radical pathway. Mechanistic investigations showed that light excitation generates from the confined NC which produces reactive oxygen species ($O_2^{\bullet-}$, $^{\bullet}OH$) that drive electron-transfer processes. DFT calculations further supported a radical mechanism and highlighted the role of multiple Cu(I) centers in enabling efficient charge separation. Thus, simply confining a Cu NC can activate its surface and impart exceptional catalytic reactivity.

Beyond confinement, introducing defects on the NC surface can also strongly influence catalytic activity. This effect was clearly demonstrated by Dong *et al.*, who showed that single-atom surface engineering can markedly enhance catalytic performance while preserving the overall structural integrity of the Cu NC.[80] They synthesized the parent $[Cu_{58}H_{20}(PET)_{36}(PPh_3)_4]^{2+}$ ($Cu_{58}H$) (PET = phenylethanethiolate; PPh_3 = triphenylphosphine) NC, *via* an optimized reduction protocol. The $Cu_{58}H$ NC features a five-shell concentric architecture surrounding a Cu_8 cubic core. Within this framework, the outermost metal–ligand shell contains a Cu_8 cube bound to four PPh_3 ligands. Based on the coordination pattern, the PPh_3 ligands bind in a μ_1 mode, leaving four surface Cu atoms coordinatively accessible and thus more susceptible to selective surface modification. Utilising this feature, the authors treated the NC with excess PPh_3 (27 : 1 molar ratio), enabling the controlled removal of a single surface Cu atom and generating the defective analogue $[Cu_{57}H_{20}(PET)_{36}(PPh_3)_4]^{+}$ ($Cu_{57}H$). Structural characterization confirmed that $Cu_{57}H$ preserves the parent geometric framework with the exception of a single-atom vacancy. Accommodation of this vacancy induces subtle rearrangements in adjacent thiolate coordination. Despite the minimal structural alteration, the defect has profound electronic consequences. Fig. 2 depicts the proposed catalytic cycle for $Cu_{57}H$-mediated photoinduced azide–alkyne cycloaddition. The reaction is initiated by coordination and activation of the alkyne to generate a Cu–σ,π-alkynyl intermediate. Subsequent light-driven radical processes enable coupling with the azide, forming the triazole framework. Notably, the presence of a surface Cu vacancy in $Cu_{57}H$ promotes substrate activation and facilitates efficient regeneration of the catalytic site, thereby enhancing overall catalytic performance. DFT calculations indicated a localized region of reduced electron density at the vacancy site, while time-resolved spectroscopy revealed a significantly prolonged excited-state lifetime (248.7 ps for $Cu_{57}H$ *vs.* 108.8 ps for $Cu_{58}H$), consistent with enhanced charge separation. These effects translated directly into catalytic performance: in photoinduced azide–alkyne cycloaddition reactions, Cu_{57} achieved a 97% yield compared to 77% for $Cu_{58}H$ under identical conditions (Fig. 2). The enhanced activity arises from three key factors: (i) the vacancy generates an exposed, coordinatively unsaturated Cu site that facilitates substrate binding; (ii) local surface rearrangement produces a geometry more reminiscent of highly reactive Cu (111) facets rather than the original Cu (100)-like arrangement; and (iii) the extended charge-separated state improves photocatalytic efficiency. Mechanistic studies further supported a radical pathway, as TEMPO quenching reduced the product yield to below 10%.

2.2. Coupling reactions

2.2.1. A^3 coupling. Jia *et al.* reported tridentate N-heterocyclic carbene (NHC) ligand protected $[Cu_3(NHC)_3(PF_6)_3]$ (PF_6 = hexafluorophosphate) (Cu_3) NC, which features an unique rigid–flexible duality.[81] Strong C–Cu and N–Cu coordination maintains the triangular Cu_3 core, while reversible pyridine dissociation generates open sites for catalysis. This balance affords exceptional solution stability and sustained catalytic integrity. The Cu_3 NC proved highly efficient for three-component dehydrogenative couplings (A^3 and redox-A^3), delivering propargylamines and C1-propargylamines—key motifs in drug synthesis—with yields up to 99% at room temperature (Fig. 3a). Conventional Cu salts and other Cu_3 NCs (*e.g.*, BINAP- or pyrazolyl-based systems) showed far lower activity, underscoring the strength of the NHC ligand design. A broad substrate scope was demonstrated across diverse aldehydes, alkynes, and secondary amines; primary amines were unreactive. Notably, reactions with 1,2,3,4-tetrahydroisoquinoline (THIQ) enabled both propargylamine and C1-propargylamine formation, with redox-A^3 couplings achieving turn over number (TONs) up to 1840 and complete regioselectivity at catalyst loadings as low as 0.025 mol% (Fig. 3b). Mechanistic studies revealed that ligand-arm dissociation exposes Cu sites for acetylide formation, which then couples with iminium intermediates. DFT showed lower activation barriers for the redox-A^3 pathway due to the *endo*-iminium intermediate, explaining its superior selectivity. The catalyst also performed well in gram-scale reactions, tolerated complex bioactive substrates, and retained activity over multiple cycles. Thus, this work

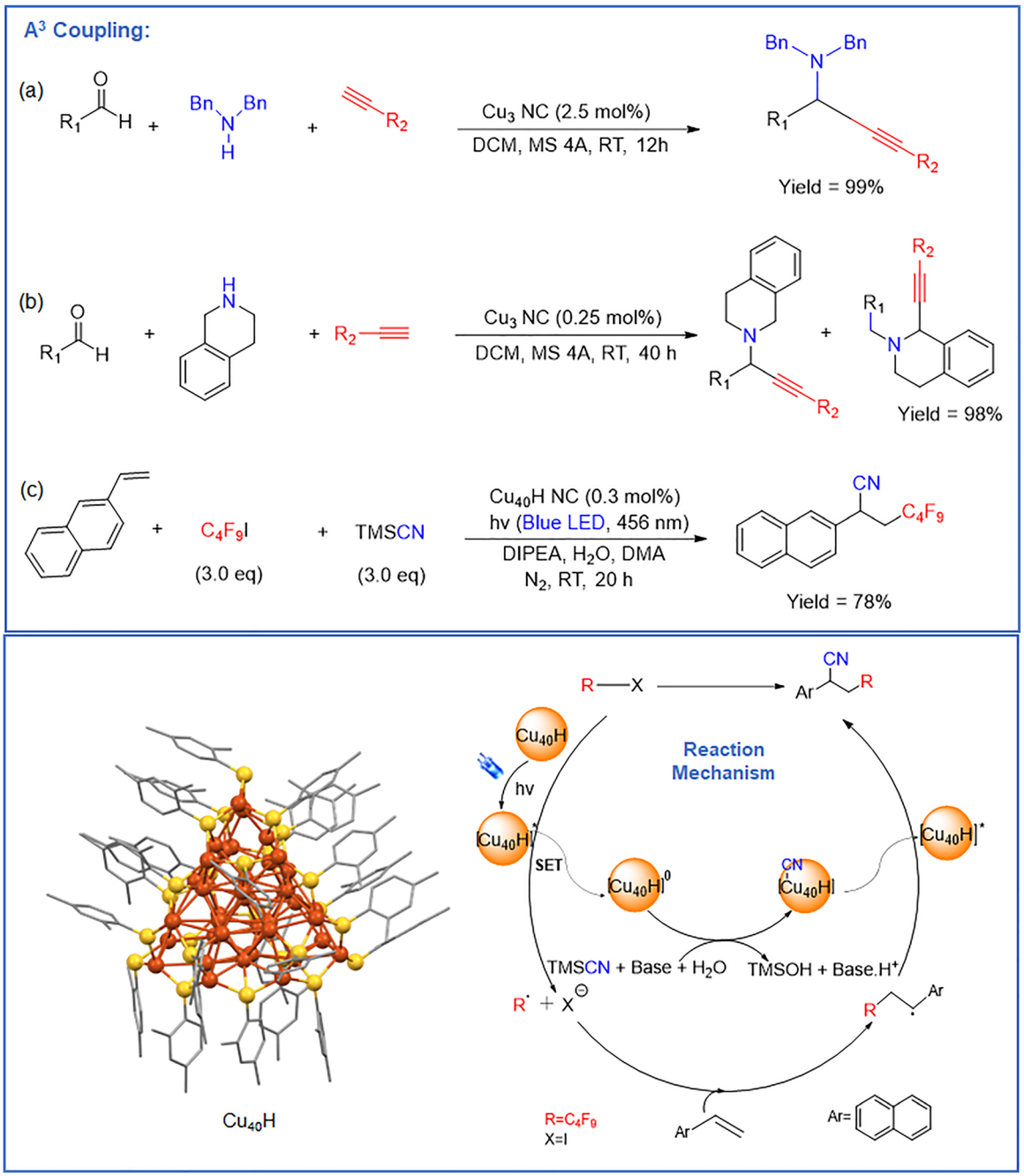

Fig. 3 Representation of the A^3 reaction and the performance of various Cu NCs, showing the corresponding yields: (a) and (b) reactions catalyzed by Cu_3 NCs, and (c) reactions catalyzed by $Cu_{40}H$ NCs and associated reaction mechanism in details by utilising $Cu_{40}H$ NC.

establishes Cu NC as a robust, dynamically adaptive platform for mild, selective A^3 coupling reaction. Later, Liu *et al.* recently reported $[Cu_{40}H_{17}(2,4\text{-DMBTH})_{24}]$ ($Cu_{40}H$) (2,4-DMBTH = 2,4-dimethylbenzenethiolate) NC and identified its catalytic activity in A^3 coupling reaction (Fig. 3c).[82] The structure comprises a Cu_{28} propeller-like core, a Cu_9 pedestal, and a Cu_3 belt, all protected by 2,4-DMBTH ligands. Multiple hydrides (μ_3-H, μ_4-H, μ_5-H) were confirmed by Electrospray Ionization – Mass Spectrometry (ESI-MS), Nuclear Magnetic Resonance (NMR), and DFT. The cluster shows strong UV-vis absorption and near infrared-II (NIR) emission (1000–1174 nm) arising from ligand to metal charge transfer (LMCT) states. Catalytically, $Cu_{40}H$ NC functions as an intrinsic photo redox catalyst capable of single-electron transfer (SET) without external ligand activation. Under blue LED light (456 nm), the excited cluster reduces perfluoroalkyl iodides (*e.g.*, C_4F_9I) to give fluoroalkyl radicals. Using this reactivity, the authors developed a three-component cyanofluoroalkylation of alkenes with perfluoroalkyl iodides and trimethylsilyl cyanide (TMSCN) in the presence of *N*,*N*-diisopropylethylamine (DIPEA) and water. As illustrated in

Fig. 3c, the A^3 coupling proceeds *via* initial ligand dissociation, generating an exposed Cu active site that facilitates the formation of a Cu–acetylide intermediate. Concurrently, condensation of the aldehyde and amine yields an iminium species, which subsequently undergoes nucleophilic addition with the Cu–acetylide to afford the propargylamine product. The catalytic cycle is completed by regeneration of the active Cu site, highlighting the dynamic ligand behavior and accessibility of reactive sites in the nanocluster. Notably, while Cu_3 follows a classical polar A^3 pathway, $Cu_{40}H$ NC system can operate *via* photoinduced single-electron processes, highlighting the mechanistic diversity accessible within atomically precise Cu NCs. All components were essential, and conventional Cu(I)/Cu(II) salts were far less effective. Even at 0.15 mol% loading, the cluster achieved TONs up to 440. The reaction showed broad substrate scope: various styrene, aliphatic and heteroaryl alkenes worked well, and a range of fluoroalkyl iodides (CF_3I to $C_8F_{17}I$) were competent electrophiles. α,α-Difluoro carbonyl compounds and products from α-bromo isobutyric ester were also accessible. Mechanistically, photoexcited $Cu_{40}H$ reduces the fluoroalkyl iodide to generate radicals and a mixed-valence NC. Radical addition to the alkene forms a C-centered radical that then couples with a cyanide-ligated Cu intermediate (from TMSCN), releasing the product and regenerating the NC. Air quenches the reaction, consistent with a radical pathway. So, $Cu_{40}H$ acts as a robust, NIR-II emissive, and intrinsically photoactive catalyst for visible-light-driven radical coupling reactions.

2.2.2. C–C coupling. Nematulloev *et al.* reported a defect-engineered defect-induced $[Cu_{28}H_{10}(4\text{-MBT})_{18}(PPh_3)_3]$ ($Cu_{28}H$) (4-MBT = 4 methylbenzenethiolate) NC, elucidated its atomic structure and catalytic behavior.[83] This work demonstrates that a single, well-defined surface vacancy can precisely regulate NC reactivity, providing a molecular-level platform to correlate defects with catalytic function. $Cu_{28}H$ NC was synthesized on a gram scale *via* a one-pot reduction of $[Cu(CH_3CN)_4]BF_4$ with sodium borohydride ($NaBH_4$) in the presence of *o*-thiocresol and PPh_3 under ambient conditions. Single-crystal X-ray diffraction reveals a distorted tetrahedral architecture consisting of a Cu_{13} anti-cuboctahedral core and a $Cu_{15}S_{18}P_3$ shell, with one Cu atom and one PPh_3 ligand missing from a vertex, creating a surface vacancy. DFT calculations show that the vacancy localizes the highest occupied molecular orbital (HOMO) on surface ligands while the Lowest unoccupied molecular orbital (LUMO) remains cluster-centered, favoring ligand-to-cluster charge transfer upon photoexcitation. $Cu_{28}H$ NC exhibits excellent photocatalytic activity in Sonogashira C–C coupling between aryl iodides and terminal alkynes under blue-LED irradiation (Fig. 4). Using sodium methoxide (NaOMe) in an MeCN/DMSO (MeCN = acetonitrile; DMSO = dimethylsulphoxide) mixture, yields up to 82% were achieved with negligible diyne homocoupling, outperforming Cu salts and even larger CuH NCs such as Cu_{61}.

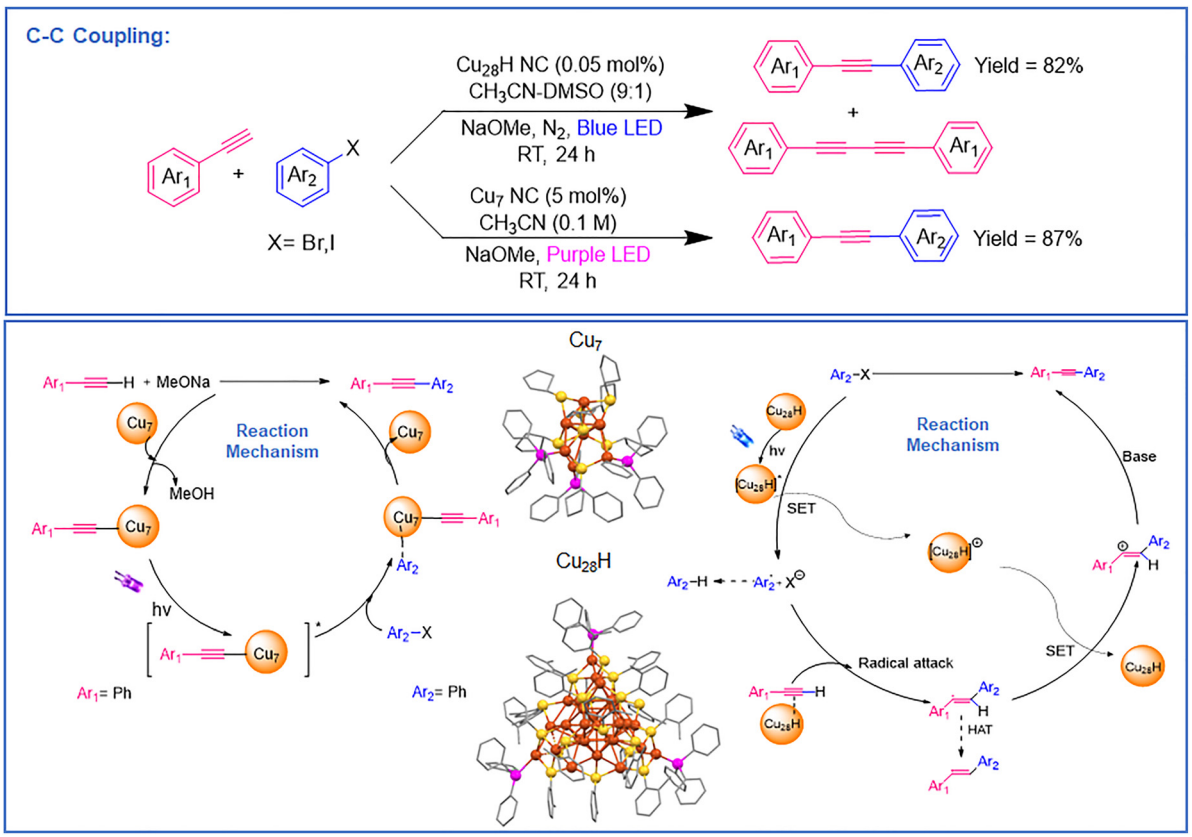

Fig. 4 Representation of C–C coupling reaction and the performance of various Cu NCs with corresponding yields with associated reaction mechanisms.

Broad substrate tolerance was observed for electronically diverse aryl iodides and alkynes, with high chemoselectivity and suppression of Glaser-type side reactions. As illustrated in Fig. 4, the $Cu_{28}H$ NC operates *via* a photoinduced radical pathway. Upon blue-light irradiation, the excited $Cu_{28}H$ species undergoes single-electron transfer (SET) with the aryl iodide to generate an aryl radical. This reactive intermediate subsequently adds to the alkyne to form a vinyl radical species, which undergoes further transformation to yield the C–C coupled product. The catalytic cycle is completed through regeneration of the ground-state $Cu_{28}H$ NC, highlighting its role as an efficient photoredox catalyst. So, this study establishes atomically precise, defect-containing Cu NCs as highly selective photocatalysts and highlights surface-vacancy engineering as a powerful strategy to tune electronic structure and catalytic performance. Later, Biswas *et al.* synthesized a hydride-free luminescent $[Cu_7(CPT)_7(PPh_3)_3]$ (Cu_7) (CPT = cyclopentathiol) NC and identified its highly selective $C(sp^2)$–C(sp) bond formation (Sonogashira-type cross-coupling) under purple LED irradiation (Fig. 4).[84] The NC contain a heptanuclear Cu_7 core with $P6_3$ symmetry and strong Cu–Cu cuprophilic interactions forming an irregular tetrahedral geometry capped by thiolates and phosphine ligands. A model reaction between iodobenzene (C_6H_5I) and HC≡CPh in the presence of 5 mol% Cu_7 NC and NaOMe in MeCN produced 1-phenyl-2-phenylacetylene in 87% yield. Substituting purple LEDs with blue LEDs or CFL bulbs reduced the yield to 79% and 43%, respectively. Replacing the NC with CuCl gave a 37% yield accompanied by homocoupled 1,3-diyne byproducts, highlighting its selectivity. To rationalize this behavior, the proposed catalytic cycle is illustrated in Fig. 4 which depicts the hydride free Cu_7 NC follows a polar catalytic pathway initiated by the formation of a Cu–σ-alkynyl intermediate upon alkyne activation. Subsequent photoexcitation enables oxidative addition of the aryl halide at the Cu center, identified as the rate-determining step, leading to a Cu–C intermediate. This is followed by reductive elimination to yield the $C(sp^2)$–C(sp) coupled product, with regeneration of the active Cu_7 NC catalyst completing the catalytic cycle. Absence of light, base, or catalyst resulted in no reaction. The catalyst was recyclable up to 10 runs with 61% yield retained, and post-catalysis UV-vis/transmission electron microscopy (TEM)/ESI-MS confirmed the overall structural integrity, though minor ligand loss occurred through PPh_3 ligands. Substrate scope tests showed that both aryl iodides and aryl bromides bearing electron-donating (–CH_3, –OCH_3) or electron-withdrawing (–NO_2, –CO_2Et, –CF_3, –F) substituents yielded corresponding alkynylated products in high selectivity. For example, *p*-nitroiodobenzene with HC≡CPh produced 4-nitrophenylphenylacetylene, while 2-bromopyridine yielded 2-(phenylethynyl)-pyridine. Similarly, various alkynes such as *p*-tolylacetylene, *p*-aminophenylacetylene, *p*-trifluoromethylphenylacetylene, and 2-thiophenylacetylene gave their respective $C(sp^2)$–C(sp) coupled products in good yields, confirming broad substrate tolerance and full suppression of alkyne homocoupling. Mechanistic studies combining radical-trapping and DFT calculations established a non-radical, polar pathway distinct from the previous study. DFT calculation revealed that the active Cu site lies at the triangular base of the Cu_4 head, where adsorption of HC≡CPh and NaOMe forms a Cu–acetylide intermediate (Cu–C ≈ 1.90 Å, ΔG = –1.06 eV). Subsequent oxidative addition of aryl iodide at this Cu center (rate-determining, $\Delta G^{\ddagger}$ = 1.15 eV) leads to a Cu(III)-like intermediate, followed by reductive elimination generating the cross-coupled product and regenerating Cu_7. The overall reaction free energy is –2.28 eV, confirming strong thermodynamic favorability. The mechanistic cycle thus proceeds *via* Cu-σ-alkynyl intermediate → photoexcited Cu-acetylide → oxidative addition → reductive elimination, forming the $C(sp^2)$–C(sp) bond cleanly through a polar process. Thus, this work demonstrates that hydride-free Cu NCs enable efficient and highly selective C–C bond formation under mild conditions. The absence of hydrides shifts the mechanism from a radical to a polar pathway, affording clean, high-yield Sonogashira-type couplings and highlighting hydride-free Cu NCs as promising catalysts for sustainable photochemical synthesis.

2.2.3. C–N coupling. Lee *et al.* reported a $[Cu_{32}H_8(PET)_{24}Cl_{22}]$ ($Cu_{32}H$) NC and identified its C–N coupling reactivity (Fig. 5a).[85] SCXRD data revealed a bisquare antiprismatic $Cu_{14}H_8$ core capped by two $Cu_7(PET)_{11}Cl$ units and two Cu_2PET units, all stabilized by hydrides and chlorides. Electronic analysis showed a zero-free-electron configuration with a ∼1.7 eV HOMO–LUMO gap, consistent with its UV-vis spectrum. DFT also explained the Cl/H exchange detected in mass spectrometry. Catalytically, $Cu_{32}H$ NC promoted carbonylation of aniline, *p*-toluidine, and 4-bromoaniline with Diisopropyl Azodicarboxylate (DIAD) in $CDCl_3$ at room temperature, giving the corresponding carbamates in high conversion (isolated yields: 60.5%, 47.4%, and 46.7%). In contrast, CuI and CuPET led to full substrate conversion but only trace carbamate formation, indicating that $Cu_{32}H$ provides unique surface interactions that selectively channel radical intermediates toward C–N bond formation. The mechanism involves DIAD decomposition into oxyacyl radicals on the Cu surface, followed by controlled coupling with aniline radicals on the NC interface. Later, Das *et al.* reported $[Cu_{29}H_{10}(S^tBu)_{12}(PPh_3)_4Cl_6][BF_4]$ ($Cu_{29}H$) NC and studied its catalytic activity for homogeneous carbonylative C–N coupling reaction (Fig. 5b and c).[86] The structure features a $Cu@Cu_{12}$ core encased in a $Cu_{16}S_{12}P_4Cl_6$ shell with ten hydrides. Chloride ligands and solvent polarity were shown to be crucial for stabilizing this architecture, distinguishing it from earlier Cu_{29}-Adm (Adm: adamantanethiolate) NCs. $Cu_{29}H$ NC is highly stable under ambient and photochemical conditions and displays UV-vis absorptions at 325, 445, and 527 nm, supported by TD-DFT. A notable electronic feature is its shell–core orbital separation, with filled orbitals on the shell and empty orbitals on the core, which underlies its catalytic reactivity. In the presence of $Cu_{29}H$ NC aniline and DIAD reacted smoothly in $CDCl_3$ at room temperature to form the corresponding carbamate in good yield, whereas CuI salts and precursor mixtures gave <5–11% yields, showing that the

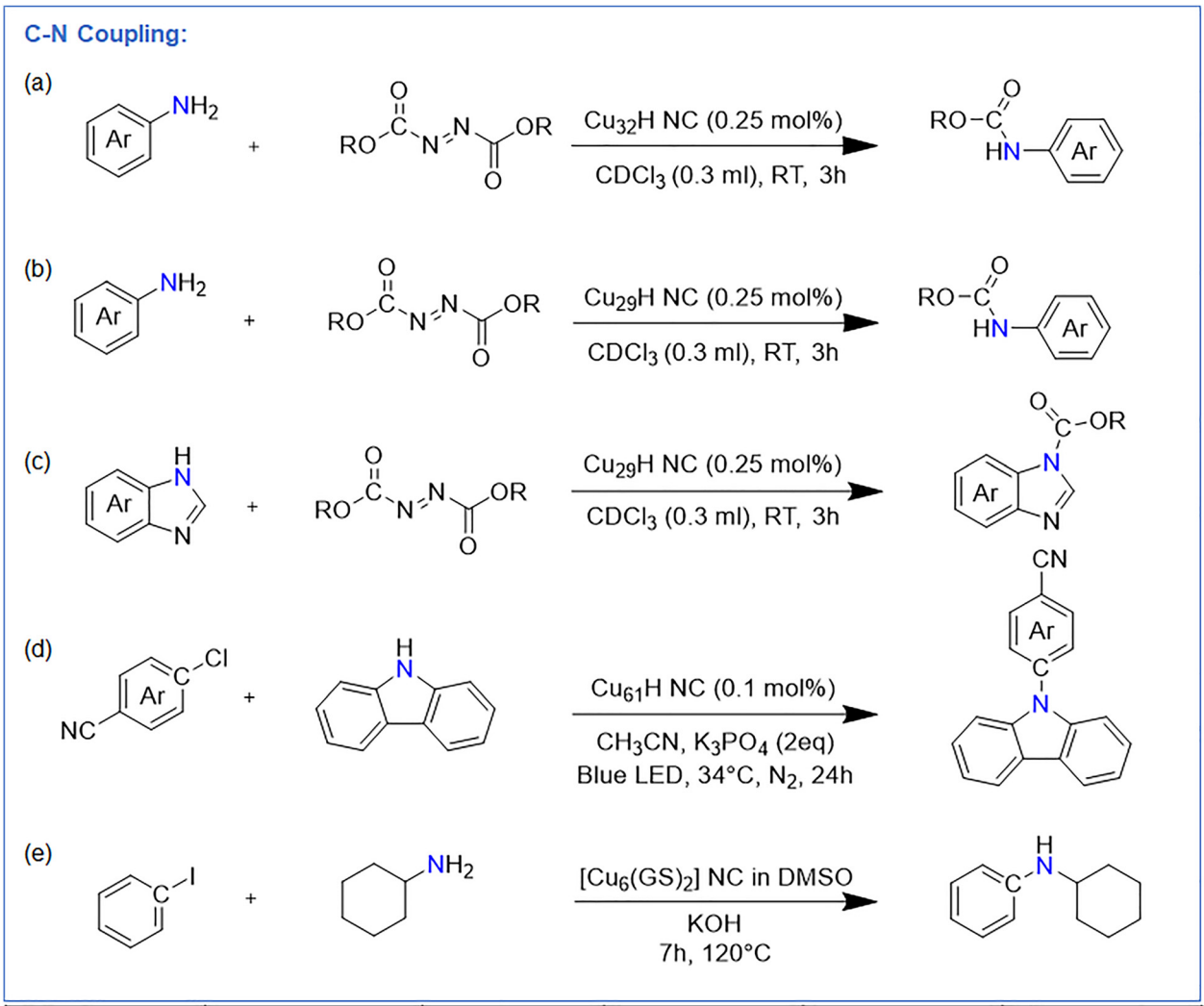

Reaction Scheme	Catalyst	Loading (mol %)	Time (h)	Temperature (°C)	Yield (%)
a	$Cu_{32}H$ NC	0.036	3	23	60.5
b	$Cu_{29}H$ NC	0.25	3	RT	71
c	$Cu_{29}H$ NC	0.25	3	RT	73
d	$Cu_{61}H$ NC	0.1	24	34	85
e	$[Cu_6(GS)_2]$ NC	2	7	120	95

Fig. 5 Representation of C–N coupling reaction and the performance of various Cu NCs with corresponding yields. The reaction is catalyzed by (a) $Cu_{32}H$, (b) $Cu_{29}H$ NC, (c) $Cu_{29}H$ NC, (d) $Cu_{61}H$ NC and (e) $[Cu_6(GS)_2]$ NC.

presence of NC is essential. Most interestingly, compared with the previous example, this study demonstrates a significantly higher yield of 71% (Fig. 5b). A range of substituted anilines (*p*-Me, *p*-^{t}Bu, 3,5-Me_2, *p*-Cl, *p*-Br) furnished carbamates in 62–78% yields, and 2-aminopyridine gave 47%. Benzimidazole also reacted with various azodicarboxylates to afford products in 59–73% yields. $Cu_{29}H$ NC outperformed the related Cu_{32} NC (59% *vs.* 46.7%). Both $Cu_{32}H$ and $Cu_{29}H$ NCs follow a similar radical-mediated C–N coupling pathway involving DIAD activation, aminyl radical formation, and radical coupling to form carbamates, with the NC surface acting as both the activation platform and stabilization environment for key intermediates. The shared mechanistic features of $Cu_{32}H$ and $Cu_{29}H$ NCs are summarized in Fig. 6. Mechanistic studies using TEMPO and 1,1-diphenylethene supported a radical pathway. Theoretically calculated free-energy profiles indicated that DIAD decomposes on $Cu_{29}H$ NC *via* N_2 extrusion to form two oxyacyl radicals, which abstract H-atoms from anilines to generate aminyl radicals. Radical–radical coupling forms the carbamate. The rate-determining DIAD decomposition is stabilized by

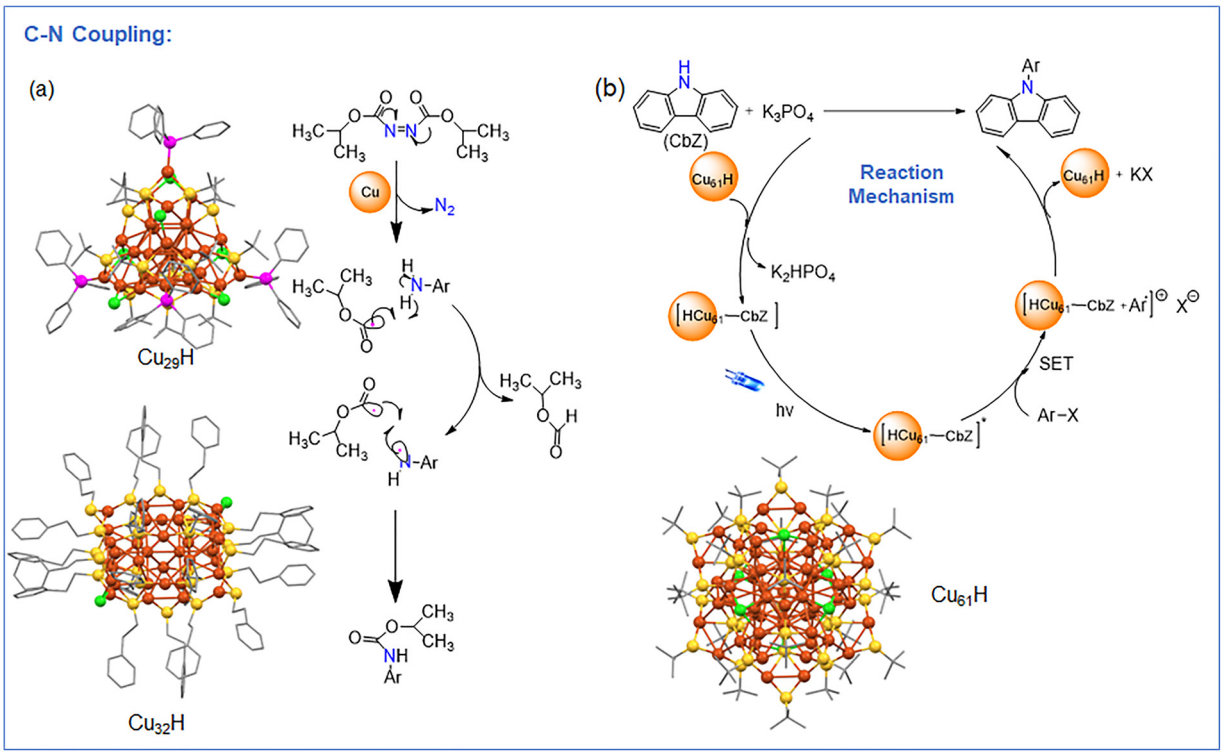

Fig. 6 Reaction mechanism of C–N coupling (a) $Cu_{29}H$ and $Cu_{32}H$ NCs have been utilized as the catalyst and (b) $Cu_{61}H$ NC has been utilized as the catalyst.

H-bonding interactions (2.8–3.1 Å) between DIAD and chloride ligands, while multiple Cl bridges increase the number of active sites. The overall process is exergonic (ΔG = –2.95 eV). Post-reaction analysis confirmed that $Cu_{29}H$ retains its structure and hydrides, demonstrating stability and recyclability. While Sagadevan *et al.* reported $[Cu_{61}H_{14}(S^tBu)_{26}S_6Cl_6]$ ($Cu_{61}H$) NC that efficiently catalyzes visible-light-induced C–N coupling of aryl chlorides at room temperature—addressing the long-standing difficulty of activating aryl chlorides under mild conditions (Fig. 5d).[87] Control experiments confirmed that neither CuCl nor standard bases/solvents could replicate its catalytic performance. $Cu_{61}H$ NC enabled coupling of carbazole with *p*-bromobenzonitrile in 88% yield and, notably, activated aryl chlorides such as *p*-chlorobenzonitrile to give 85% yield under the same conditions. The catalyst showed broad substrate scope: electron-poor aryl chlorides reacted efficiently, electron-rich ones gave moderate yields, and sterically hindered halides, naphthyl derivatives, heteroaryl chlorides (pyridines, benzoxazoles, thiophenes), and bromoquinolines all provided arylamines in 69–87% yield. A wide range of N-heterocycles (carbazoles, indoles, azaindoles, benzimidazoles) were also successfully aminated. In contrast to $Cu_{32}H$ and $Cu_{29}H$, $Cu_{61}H$ NC operates *via* a photoinduced single-electron transfer (SET) pathway (Fig. 6). Upon visible-light irradiation, the $Cu_{61}H$ NC forms an excited-state Cu–amine complex capable of transferring an electron to the aryl halide, generating an aryl radical intermediate. This radical subsequently couples with the Cu-bound amine species to form the C–N bond, followed by regeneration of the ground-state nanocluster. The process highlights the role of the nanocluster as a photoredox catalyst, where light excitation enables activation of otherwise inert aryl halides under mild conditions. Mechanistic studies supported a SET pathway rather than classical oxidative addition. Radical clock experiment indicated aryl radical intermediates, and photophysical studies (Photoluminescence (PL) quenching, lifetime measurements) verified SET from the photoexcited $Cu_{61}H$ NC–carbazolide complex to the aryl halide. The resulting aryl radical then coupled with the Cu–amine intermediate to regenerate the catalyst. On the other hand, Mondal *et al.* reported water soluble glutathione-protected $[Cu_6(GS)_2]$ NCs and demonstrated their catalytic activity in C–C and C–N bond formation (Fig. 5e).[88] Using only 2 mol% catalyst, $[Cu_6(GS)_2]$ promoted Ullmann-type $C(sp^2)$–$C(sp^2)$ coupling of aryl iodides to afford a range of biphenyl derivatives (unsubstituted, methyl-, methoxy-, acetyl-, and hydroxy-substituted biphenyls). The clusters also enabled Buchwald–Hartwig-type $C(sp^2)$–$N(sp^3)$ coupling between aryl iodides and cyclohexylamine, giving secondary aryl-cyclohexylamines in high yields. All reactions proceeded efficiently in DMSO at 120–160 °C, showing far higher activity at low loadings than traditional Cu or Pd catalysts. Mechanistic matrix-assisted laser desorption/ionization time-of-flight (MALDI–TOF) analysis detected intermediates such as $[Cu_6(GS)_2Ph + Na]^+$ and $[Cu_6(GS)_2Ph_2 + K]^+$ during C–C coupling and only $[Cu_6(GS)_2Ph + Na]^+$ for C–N coupling, indicating stepwise phenyl coordination to the cluster. DFT studies supported a classical Ullmann pathway: oxidative addition of iodobenzene (rate-limiting), followed by a second oxidative addition and reductive elimination to form

biphenyl. Polar DMSO stabilized oxidative addition steps, and catalyst regeneration was exothermic. Compared with Au clusters, CuNCs more favorably mediate C–I cleavage and C–C bond formation.

2.3. Hydroboration

Alamer *et al.* reported a robust $[Cu_{45}H_{14}(TBBT)_{29}(PPh_3)_4(^tBuNH_2)_2]^{2+}$ ($Cu_{45}H$) (TBBT = 4-*tert*-butylbenzenethiolate; $^tBuNH_2$ = *tert*-butylamine) NC, featuring a planar hexagonal Cu_7 core enclosed by a Cu_{38} shell composed of two Cu–thiolate layers linked through a phosphine-stabilized macrocyclic $Cu_{14}(TBBT)_{16}P_4$ ring.[89] The NC contains 14 hydrides and is structurally well-defined by SCXRD. $Cu_{45}H$ proved to be a highly efficient catalyst for hydroboration of C–C multiple bonds, delivering up to 90% isolated yield and >95% *E*-selectivity for terminal alkynes at only 0.025 mol% loading under ambient, open-air conditions (Fig. 6). Air and water were beneficial to the catalytic cycle, and control studies identified the macrocyclic Cu–S–P interface as the active site, outperforming Cu–TBBT, Cu–TPP, $Cu_{61}H$, and even CuCl (5 mol%). The catalyst tolerated diverse functional groups and showed broad substrate scope, including aryl, heteroaryl, and aliphatic alkynes, internal alkynes, and styrenes, with recyclability up to five cycles and gram-scale applicability. As shown in Fig. 7, the $Cu_{45}H$ NC catalyzes hydroboration *via* a radical-mediated pathway. Activation of the boron reagent at the Cu–thiolate–phosphine interface generates reactive radical species, which subsequently add across the C≡C bond of the alkyne to form a vinyl intermediate. This intermediate undergoes further transformation to yield the hydroborated product with high regio- and stereoselectivity. The catalytic cycle is sustained by regeneration of the active $Cu_{45}H$ NC, with the cluster interface playing a crucial role in facilitating substrate activation and stabilizing reactive intermediates. Mechanistic experiments indicated a radical pathway, supported by inhibition with TEMPO/BHT/DMPO (BHT = butylated hydroxytoluene; DMPO = 5,5-dimethyl-1-pyrroline N-oxide) and detection of radical adducts by GC–MS. Thus, $Cu_{45}H$ NC demonstrates

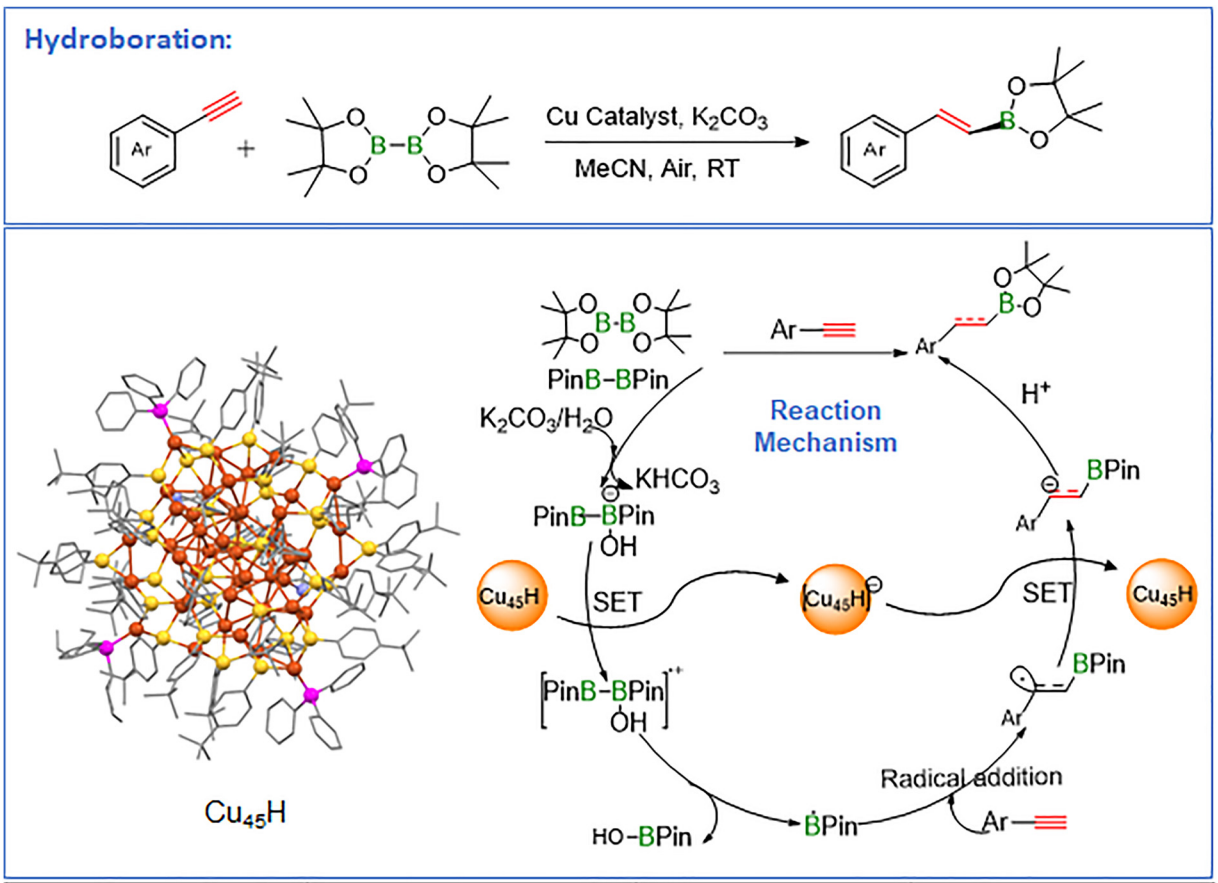

Catalyst	Loading (mol %)	Time (h)	Yield (%)
$Cu_{45}H$ NC	0.025	5	84
Cu_4 NC	2	1	98

Fig. 7 Representation of hydroboration reactions and the performance of various Cu NCs with corresponding yields.

how precise Cu–thiolate–phosphine interfaces in atomically defined clusters enable highly selective C–B bond formation under mild conditions.

Jia *et al.* reported dual catalytic sites for highly chemoselective alkyne hydroboration in synthesized NCs.[90] They reported ($[Cu_4(NHT)_4]$) (Cu_4) NC and $[Cu_8(NHT)_4(S^tBu)_4]$ (Cu_8) (NHT = N-heterocyclic thione; S^tBu = *tert*-butyl thiolate) in which N-heterocyclic thione ligands provide both strong Cu–S and reversible Cu–N coordination. SCXRD revealed a Cu_4 core bridged by NHT ligands in Cu_4 NC and a fused Cu_4–Cu_4 architecture in Cu_8 NC. This combination of structural stability and dynamic Cu–N flexibility enabled efficient heterogeneous catalysis under ambient conditions. Cu_4 NC showed exceptional hydroboration activity with bis(pinacolato)diboron (B_2Pin_2), delivering vinylboronates in up to 98% yield and achieving a TON of 77 786—far exceeding conventional Cu catalysts (Fig. 6). It exhibited excellent regio-, stereo-, and chemoselectivity across diverse aryl, heteroaryl, and sterically hindered alkynes, preferentially reducing C≡C bonds even in the presence of alkenes or carbonyls. Cu_8 NC, in contrast, showed only moderate activity (64% yield). Mechanistic studies indicated that reversible Cu–N bond dissociation generates open active sites, while robust Cu–S bonds maintain cluster integrity. The reaction proceeds *via* cluster borylation, alkyne insertion, and protonation. DFT results showed a lower activation barrier for Cu_4 NC (22.9 kcal mol^{-1}) than for Cu_8 NC (24.7 kcal mol^{-1}), rationalizing its superior reactivity.

2.4. Hydrogenation

Sun *et al.* reported the hydride-rich $[Cu_{25}H_{10}(SPhCl_2)_{18}]^{3-}$ ($Cu_{25}H$), featuring a Cu_{13} icosahedral core capped by twelve Cu atoms and stabilized by ten hydrides and eighteen thiolates.[91] This atomically precise NC exhibits remarkable catalytic activity for the room-temperature hydrogenation of 2-hexanone and 3-hexanone to the corresponding alcohols (Fig. 8a). Notably, D_2-labeling experiments unambiguously revealed that the hydride ligands themselves act as the hydrogen source, directly transferring hydrogen to the substrate during reduction. Consequently, the hydrides play a dual role: they not only stabilize the Cu framework but also constitute a readily accessible and reactive hydride reservoir. Importantly, SCXRD and ESI-MS analyses confirmed that the NC structure remained intact after catalysis. This unique structural and functional synergy endows $Cu_{25}H$ NC with distinctive single-site catalytic behavior and underpins its high efficiency in selective hydrogenation reactions.

Later, Lan *et al.* reported an efficient catalytic system for converting levulinic acid to γ-valerolactone using Cu NCs stabilized by graphitic carbon nitride (g-C_3N_4) within Santa Barbara Amorphous-15 (SBA-15) mesoporous silica to check the effectivity in heterogenous medium.[92] The catalyst, Cu/NC@SBA-15, prepared through impregnation, calcination, and H_2 reduction, benefits from *in situ*-formed g-C_3N_4, whose N–Cu coordination stabilizes mixed-valent $Cu^0/Cu^+/Cu^{2+}$ sites and suppresses agglomeration. Cu/NC@SBA-15 delivered 92% yield at 140 °C and 3 MPa H_2—comparable to Ru catalysts—and remained highly effective under milder conditions (93% conversion at 120 °C; 53% yield at 0.1 MPa H_2) (Fig. 8b). It exhibited a high TOF (5.42 h^{-1}), low activation energy (35.6 kJ mol^{-1}), and outstanding durability, maintaining activity for 100 h of continuous operation. DFT calculations revealed that the key hydrogenation step proceeds with a significantly lower barrier on Cu NCs (1.12 eV) than on extended Cu surfaces (1.93 eV), attributed to abundant low-coordination edge/corner sites. Combined effects of N–Cu stabilization, and mesoporous confinement enhance H_2 activation and C=O hydrogenation. Thus, hydrogenation can be achieved using Cu NCs under both homogeneous and heterogeneous conditions. However, variations in their structural architecture play a crucial role in determining their hydrogenation activity. Such effect is visible when Dong *et al.* reported an atomically precise chiral Cu NC, $[Cu_{18}H(PET)_{14}(PPh_3)_6(NCS)_3]$ ($Cu_{18}H$) (NCS = isothiocyanate), featuring a Cu_{15} triple-helical core stabilized by PET, PPh_3, and NCS ligands with one hydride.[93] Structurally, $Cu_{18}H$ forms a three-layer chiral sandwich, which packs in the crystal as CCC- and AAA-enantiomers that assemble into a double-helical supramolecular structure supported by C–H···H–C, C–H/π, and C–H/S contacts. Catalytically, Cu_{18} shows exceptional electron-transfer activity in reducing $[Fe(CN)_6]^{3-} \rightarrow [Fe(CN)_6]^{4-}$. Without the NC, the $NaBH_4$-driven reduction requires ∼16 min, whereas $Cu_{18}H$ NC accelerates it to 14 s. The tightly packed double helix provides extended pathways for electron delocalization, analogous to DNA-mediated transfer, while the hydride ligand may assist in electron shuttling. UV-vis analysis confirmed that the cluster remains intact after reaction, highlighting its robustness and recyclability. So, $Cu_{18}H$ NC functions as a highly efficient electron-transfer catalyst, where 3D chirality and double-helical assembly directly enhance stability and reactivity.

Luo *et al.* reported another chiral $[Cu_{57}H_{20}(PET)_{36}(PPh_3)_4]$ ($Cu_{57}H_{20}$) NC and assessed its reactivity for hydrogenation reaction (Fig. 8c).[94] SCXRD showed a Cu_8 cubic core encapsulated by a $Cu_{49}(PET)_{36}(PPh_3)_4$ shell that contains a single Cu vacancy, creating a mono-lacunary defect analogous to polyoxometalates. This missing metal site exposes a μ_3-hydride on a Cu_3 triangle, a key structural feature absent in its fully occupied Ag analogue. $Cu_{57}H_{20}$ efficiently catalyzed the $NaBH_4$ mediated hydrogenation of *p*-nitrophenol to *p*-aminophenol, with the 400 nm *p*-NP band disappearing and the 300 nm product band emerging, reaching complete conversion in 20 min (k = 0.18 min^{-1}). No reaction occurred without the cluster. Post-catalysis UV-vis and TEM confirmed that the $Cu_{57}H_{20}$ NC remained intact. Although slightly slower than the smaller $Cu_{11}H_3$ catalyst, $Cu_{57}H_{20}$ significantly outperformed hydride-containing Ag clusters, highlighting the beneficial role of its vacancy defect and exposed hydride site in enabling efficient hydrogen transfer.

The effect of the structural architecture is more prominent when Liu *et al.* reported two nearly identical—$[Cu_{20}H_9(Tf\text{-}dpf)_{10}]^+$ ($Cu_{20}H_9$) and $[Cu_{20}H_8(Tf\text{-}dpf)_{10}]^{2+}$ ($Cu_{20}H_8$) (Tf-dpf = *N*,*N*′-di(5-trifluoromethyl-2-pyridyl)formamidinate) NCs—that differ by only a single hydride yet display strikingly different structures and reactivity.[95] Their catalytic behaviour was

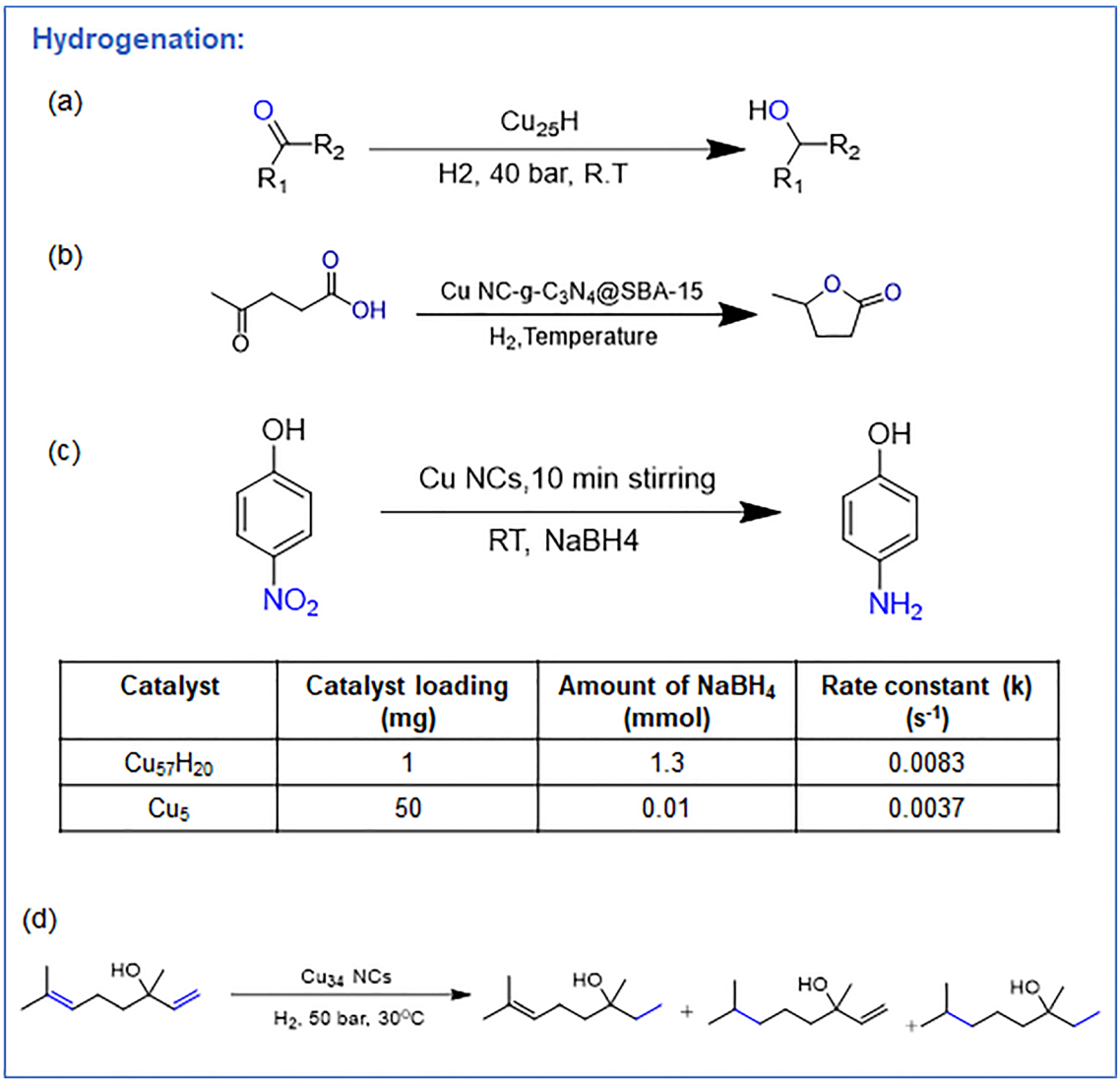

Catalyst	Catalyst loading (mg)	Amount of $NaBH_4$ (mmol)	Rate constant (k) (s^{-1})
$Cu_{57}H_{20}$	1	1.3	0.0083
Cu_5	50	0.01	0.0037

Fig. 8 (a) Representation of hydrogenation reactions with $Cu_{25}H$ NC. (b) Representation of hydrogenation reactions using Cu NCs stabilized by g-C_3N_4 within SBA-15 mesoporous silica medium for heterogenous catalysis. (c) Representation of hydrogenation reactions and the performance of various Cu NCs with corresponding yields. (d) Representation of hydrogenation reaction with Cu_{34} NC.

evaluated in the selective hydrogenation of cinnamaldehyde to 3-phenylpropanal using Ph_2SiH_2. $Cu_{20}H_8$ showed excellent performance, giving 96.7% yield at 0.2 mol% loading within 4 h, whereas $Cu_{20}H_9$ produced only 3.7%, even with increased loading or extended time. ESI-MS revealed that $Cu_{20}H_8$ undergoes partial ligand dissociation, forming species such as $[Cu_{20}H_8(Tf\text{-}dpf)_9(EtO)(EtOH)]^{2+}$ during catalysis—evidence of accessible Cu sites. In contrast, $Cu_{20}H_9$ remains fully intact, showing no ligand loss. DFT calculations support this difference: $Tf\text{-}dpf^-$ dissociation is 0.3 eV more favorable in $Cu_{20}H_8$, explaining its ability to open coordination sites for substrate activation. Thus, despite their near-identical compositions, $Cu_{20}H_8$ is catalytically active due to ligand lability, whereas $Cu_{20}H_9$ is inert because of its overly rigid coordination environment. Basu *et al.* reported a BSA-stabilized, water-soluble Cu_5 NC (<2 nm) in which Cu(I) centers are stabilized through coordination with thiol, amine, and carboxylate groups of the protein matrix.[96] The catalytic activity of the BSA–Cu NCs was evaluated for the $NaBH_4$-mediated reduction of 4-nitrophenol, where UV-vis monitoring showed the decay of the 400 nm 4-nitrophenolate band and the appearance of the 300 nm 4-aminophenol band (Fig. 8c). Li *et al.* developed an atomically precise Cu NCs featuring built-in frustrated Lewis pair (FLP) sites by anchoring methoxy-substituted thiolate ligands onto a Cu NC framework.[97] The resulting cluster, $[Cu_{34}S_7(RS)_{18}(PPh_3)_4]^{2+}$ (Cu_{34}) NC, contains a $Cu_{21}S_5$ core wrapped by a $Cu_{13}S_2(RS)_{18}$-$(PPh_3)_4$ shell. The methoxy groups create surface FLPs in which Cu(I) atoms function as Lewis acids and ligand O atoms as Lewis bases, enabling heterolytic H_2 activation without forming acid–base adducts. For catalytic testing, linalool hydrogenation was chosen because it contains two sterically distinct C=C bonds. The supported catalyst (Cu_{34}/XC-72) delivered nearly quantitative conversion with >99% selectivity to 1,2-dihydrolinalool at room temperature (Fig. 8d). Other Cu NCs capped

with nonfunctional ligands—and even a methoxy-thiolate-protected Cu_9 cluster lacking frustrated Cu–O pairs—were completely inactive, confirming the necessity of FLP sites for H_2 activation. Poisoning experiments using external Lewis acids (CO_2, pyrrole) or bases (pyridine, NH_3) strongly suppressed reactivity, verifying that Cu–O FLPs were the active centers. DFT calculations showed that hydrogenation to product A is favored by 2.95 eV and proceeds with a barrier of 2 eV lower than formation of the alternative regioisomer, explaining the exclusive selectivity. Overall, this study demonstrates that embedding FLP motifs directly onto Cu NC surfaces enables efficient and highly regioselective hydrogenation, establishing a well-defined model platform for heterogeneous FLP catalysis using earth-abundant metals.

2.5. Indolizine

Wang *et al.* reported an atomically precise pyrazolate-protected Cu_8 NC notable for its extraordinary chemical stability.[98] The D_2h-symmetric Cu_8 ring, stabilized by eight strongly coordinating μ-pyrazolate ligands, resists conditions that typically decompose Cu NCs. Remarkably, Cu_8 remained crystalline after exposure to boiling water, concentrated H_2O_2, 1 M HCl, and saturated KOH, and persisted in aerated solution for over 20 days without degradation. XPS confirmed Cu(I) retention even after months in air, and thermogravimetric analysis (TGA) indicated decomposition only near 300 °C. This exceptional robustness arises from the rigid, multidentate Cu–N coordination network and the hydrophobic ligand shell, which together block access of water, acids, bases, and oxidants to the metal core. DFT calculations further revealed a large HOMO–LUMO gap (4.63 eV), consistent with the cluster's remarkable kinetic inertness. They demonstrated its exceptional chemical robustness of Cu_8 NC enables its use as an efficient homogeneous catalyst for the three-component synthesis of indolizines (Fig. 9). With only 0.5 mol% loading, Cu_8 NC delivered high yields, whereas common Cu salts and other Cu NCs showed poor activity. The rigid pyrazolate framework imparts unusual resistance to acid, base, and oxidation, allowing Cu_8 NC to remain structurally intact under reaction conditions. This stability underpins its superior performance, enabling gram-scale synthesis with catalyst loadings as low as 0.005 mol% (97% yield) and allowing more than ten recyclings without loss of activity. The reaction exhibited broad substrate scope: aryl alkynes with both electron-donating and electron-withdrawing groups gave excellent yields, while aliphatic alkynes performed moderately due to weaker π-coordination. A wide range of secondary amines—including cyclic and drug-derived substrates—also reacted efficiently. This study demonstrates that structural design and chemical stability—not merely metal content—are decisive factors in unlocking the catalytic potential of atomically precise Cu NCs.

2.6. Oxidation

Bodiuzzaman *et al.* introduced an atomically precise Cu NC, $[Cu_{13}H_{10}(Nap)_3(PPh_3)_7]$ ($Cu_{13}Nap$) (Nap = 1-naphthalene-thiolate), as an efficient photocatalyst for decarboxylative oxygenation

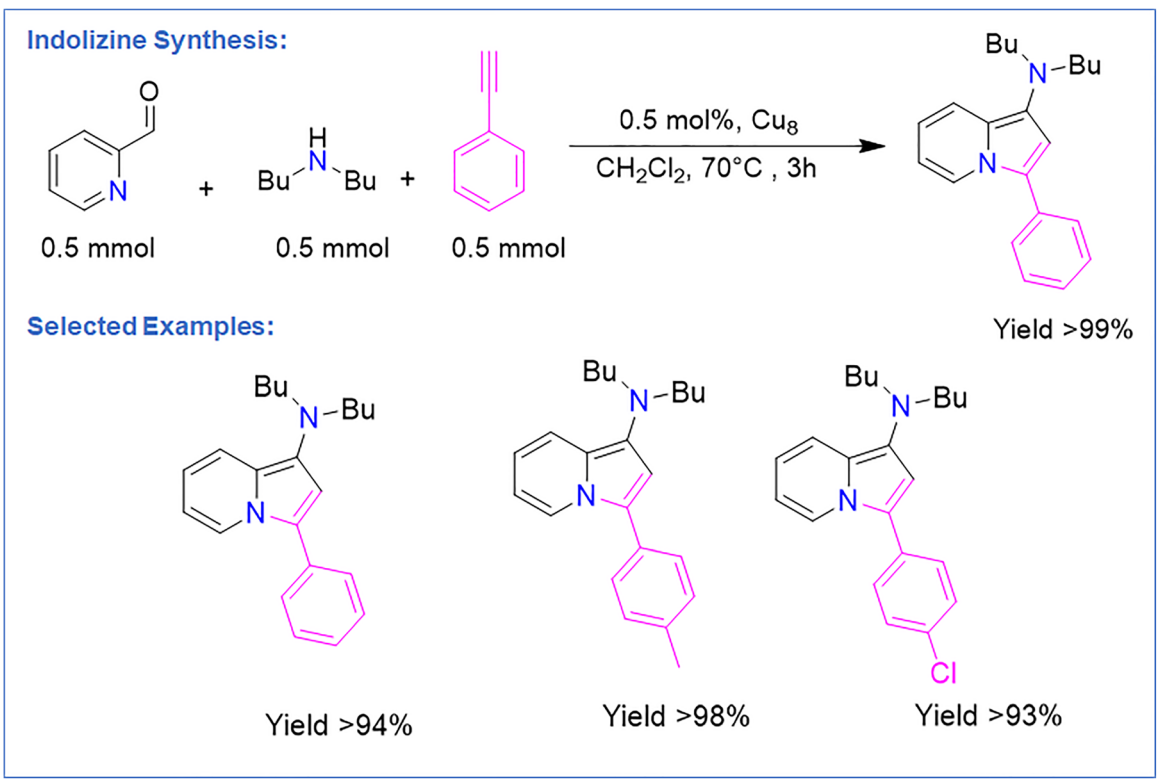

Fig. 9 Representation of indolizine reaction and the performance of Cu_8 NCs with corresponding yields by substrate variation.

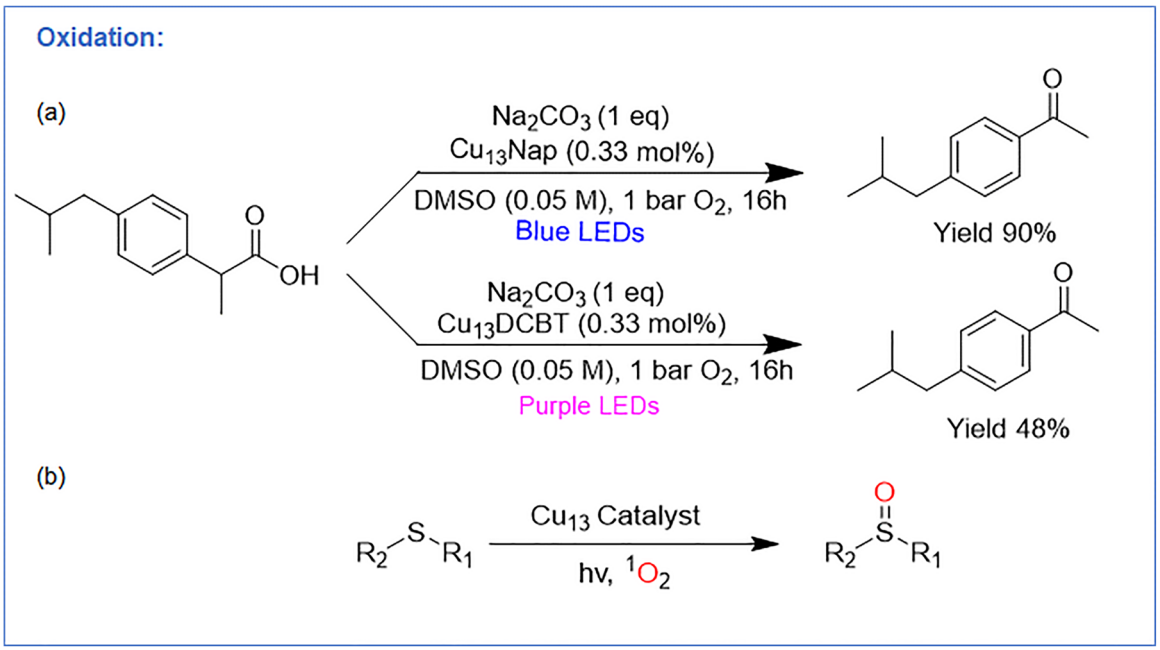

Fig. 10 Representation of oxidation reaction and the performance of two Cu_{13} NCs with corresponding yields.

under mild conditions (Fig. 10a).[99] A structurally analogous cluster, $[Cu_{13}H_{10}(DCBT)_3(PPh_3)_7]$ (Cu_{13}DCBT) (DCBT = 2,4-dichlorobenzenethiolate) served as a comparison but showed markedly lower activity (Fig. 12). Cu_{13}Nap catalyzed the decarboxylative oxidation of Ibuprofen with 0.33 mol% loading under blue-light irradiation and O_2, delivering the corresponding ketone in 90% yield. Among reported Cu NCs (Cu_{28}, Cu_{29}, Cu_{45}, Cu_{57}, Cu_{61}), Cu_{13}Nap showed the highest efficiency, whereas Cu_{13}DCBT gave only 28% yield. The NC also displayed broad substrate scope, converting primary and secondary carboxylic acids—including heteroaryl, functionalized, aliphatic, and pharmaceutical derivatives—into aldehydes or ketones in up to 94% yield. Mechanistic studies ruled out SET pathways, as the oxidation potential of Cu_{13}Nap was insufficient for direct substrate oxidation. Instead, radical traps, oxygen quenchers, NIR PL, and EPR experiments supported a singlet-oxygen ($^1O_2$) mediated mechanism. TD-DFT calculations further showed that the triplet excited state of Cu_{13}Nap efficiently sensitizes O_2 to $^1O_2$, which drives decarboxylation followed by C–O bond formation. The superior performance of Cu_{13}Nap relative to Cu_{13}DCBT was attributed to stronger visible-light absorption and longer excited-state lifetimes imparted by the naphthalene thiolate ligands. Post-reaction ESI-MS analysis confirmed that the Cu_{13}Nap NC retained its original molecular composition after 16 h of irradiation under catalytic conditions, demonstrating excellent structural stability during photocatalysis. Thus, this work establishes atomically precise Cu NCs as effective photosensitizers for $^1O_2$-mediated decarboxylative oxygenation and expands the mechanistic landscape of Cu–NC photocatalysis beyond electron-transfer pathways.

Zhang *et al.* developed a solvent-controlled route to two quasi-isomeric Cu NCs, Cu_{13}a and Cu_{13}b, stabilized by 9-(prop-2-yn-1-yl)-9*H*-carbazole (CZ-PrAH) and *p-tert*-butylthiacalix[4]arene (H_4TC_4A) ligands.[100] The isomerism arose from selective chloride release: $CHCl_3$ furnished Cu_{13}a with a coordinated Cl^- ligand, whereas CH_2Cl_2 yielded Cl-free Cu_{13}b. SCXRD showed both clusters possess similar Cu_{13} kernels with strong cuprophilic interactions, but the bound chloride in Cu_{13}a induced greater structural distortion. Electronic analyses and TD-DFT revealed that chloride incorporation generated a distinct X(Cl) → M(Cu) charge-transfer transition, narrowing the HOMO–LUMO gap and enhancing spin–orbit coupling. As a result, Cu_{13}a displayed more efficient intersystem crossing and stronger singlet-oxygen ($^1O_2$) sensitization, while Cu_{13}b mainly produced superoxide ($O_2^{\bullet-}$). Both NCs photocatalyzed aerobic sulfide oxidation with full substrate conversion (Fig. 10b). However, Cu_{13}a consistently delivered higher sulfoxide selectivity—for example, >99.9% for dimethyl sulfide compared to 93.4% for Cu_{13}b. Scavenger experiments confirmed $^1O_2$ as the dominant reactive species for Cu_{13}a, whereas $O_2^{\bullet-}$ contributed substantially in Cu_{13}b. Oxygen exclusion suppressed reactivity, verifying O_2 from air as the oxidant. Furthermore, PXRD analysis before and after catalysis confirmed that the NC framework remained unchanged, and both Cu_{13}a and Cu_{13}b maintained similar photocatalytic performance over multiple cycles, indicating good structural stability under reaction conditions. So, this study highlights how a single chloride ligand can finely modulate charge-transfer pathways, excited-state dynamics, and oxygen-species selectivity in atomically precise Cu_{13} photocatalysts.

Liu *et al.* reported the mixed-valence $[Cu_{54}S_{13}O_6(S^tBu)_{20}(^tBuSO_3)_{12}]$ (Cu_{54}) ($^tBuSO_3$ = *tert*-butanesulfonate) NC, the largest atom-precise Cu^I/Cu^{II} cluster known to date.[101] Its $Fm\bar{3}m$ cubic structure features a multilayer core–shell arrangement: a

central sulfide anion inside a $Cu_{12}O_6$ dodecahedron, surrounded by an S_{12} icosahedron, and an outer shell of 42 Cu atoms coordinated by 20 S^tBu^- and 12 $^tBuSO_3^-$ ligands. Spectroscopy indicates a Cu^I/Cu^{II} ratio of ~38 : 16 (average oxidation state +1.3). Cu_{54} NC shows broad absorption up to 580 nm with a 2.05 eV band gap. When supported on titanium dioxide (TiO_2), the composite Cu_{54}/TiO_2 exhibits excellent visible-light photocatalytic activity for phenol degradation. Upon irradiation ($\lambda > 420$ nm), phenol is rapidly converted to intermediates such as benzoquinone, hydroquinone, and catechol. The optimal 1.0 wt% Cu_{54}/TiO_2 achieves >95% phenol removal within 1.5 h, outperforming TiO_2 alone. Mechanistically, both Cu_{54} and TiO_2 are photoexcited, and because the Cu_{54} conduction band (−1.94 eV) is more negative than that of TiO_2 (−1.16 eV), electrons flow from Cu_{54} to TiO_2, generating $O_2^{\bullet-}$ for phenol oxidation. Holes in the Cu_{54} valence band (+0.11 eV) further contribute to oxidation. This efficient charge separation boosts activity, while excessive Cu_{54} loading blocks TiO_2 surface sites and lowers performance. The catalyst retains structure and activity over repeated cycles. Overall, this work establishes Cu_{54} NC as a robust mixed-valence photocatalyst and provides a promising design strategy for future Cu-based environmental catalysts.

2.7. Protosilylation

Wen *et al.* reported two atomically defined $[Cu_6(S^tBu)_2(dppm)_2(mnt)_2]\cdot CHCl_3$ (Cu_6-1) and $[Cu_6(S^tBu)_2(dppe)_2(mnt)_2]$ (Cu_6-2) (mnt = maleonitriledithiolate, dppm = (bis(diphenylphosphino)-methane), dppe = (1,2-bis(diphenylphosphino)ethane) NCs.[102] SCXRD revealed that Cu_6-1 features a fused Cu_4 tetrahedral core capped by mnt and bisphosphine ligands, leaving two Cu sites exposed for catalysis. Compared with Cu_6-2, Cu_6-1 exhibits shorter Cu···Cu distances and stronger C–H···π interactions, giving markedly enhanced structural stability. Cu_6-1 proved highly active for open-air protosilylation of C≡C and C=C bonds (Fig. 11). Using HC≡CPh, (dimethylphenylsilyl)boronic acid pinacol ester ($PhMe_2SiBpin$), 1,8-Diazabicycloundec-7-ene (DBU), and MeCN/MeOH, Cu_6-1 afforded the (E)-silylalkene in 91% yield, outperforming Cu_6-2 and larger NCs (Cu_8, Cu_{15}, Cu_{54}) or classical Cu salts. These NCs tolerated a broad substrate scope—including aryl/alkyl acetylenes, TMS-alkynes, internal alkynes, alkenes, and enynes—producing *trans*-silylalkenes, silyl-allenes, and even disilylated allenes. The catalyst was robust under gram-scale conditions, delivering TON up to 14 200 with excellent functional-group compatibility, exhibiting excellent post-catalytic stability with no detectable structural change as confirmed by UV-vis, NMR and ESI-MS analyses. Silylalkene products were easily diversified through halogenation and Pd-catalyzed coupling. Importantly, Cu_6-1 retained full activity over eight cycles with no structural change, while Cu_6-2 progressively deactivated due to weaker intracluster interactions. DFT studies supported a dual-Cu mechanism: $PhMe_2SiBpin$ first forms a Cu–Si species, followed by alkyne coordination and S^tBu dissociation. A two-Cu migratory insertion step with a low barrier (23.1 kcal mol^{-1}) accounts for the high activity and broad reactivity at room temperature.

2.8. Sulfonylation

Alotaibi *et al.* reported $[Cu_{19}H_6(S^tBuPhCH_2)_{12}(PPh_3)_6Br]$ ($Cu_{19}H$) ($S^tBuPhCH_2$ = (*tert*-butylthio)methylbenzene)) NC, featuring a Cu_{13} Ino-decahedral core capped by four ligand motifs, one bridging bromide, and six hydrides.[103] A key structural feature is that three faces of the metal core remain exposed, providing accessible Cu sites for catalysis. They utilized this $Cu_{19}H$ NC as a highly efficient visible-light photocatalyst for the sulfonylation of aryl halides. Using only 0.025 mol% catalyst, 4-bromobenzonitrile and sodium 4-methylbenzenesulfinate were converted to 4-(methylsulfonyl)benzonitrile in 88% yield under 390 nm irradiation in DMSO (Fig. 12). No reaction occurred without light or catalyst, consistent with a photo-induced SET pathway. Cu_{19} outperformed CuX (X = Cl, Br or I) salts and other Cu clusters (Cu_{28}, Cu_{29}, Cu_{45}, Cu_{58}, Cu_{61}), attributed to its unshielded Cu faces that directly interact with sulfinates. Immobilization on silica (Cu_{19}–S) enabled

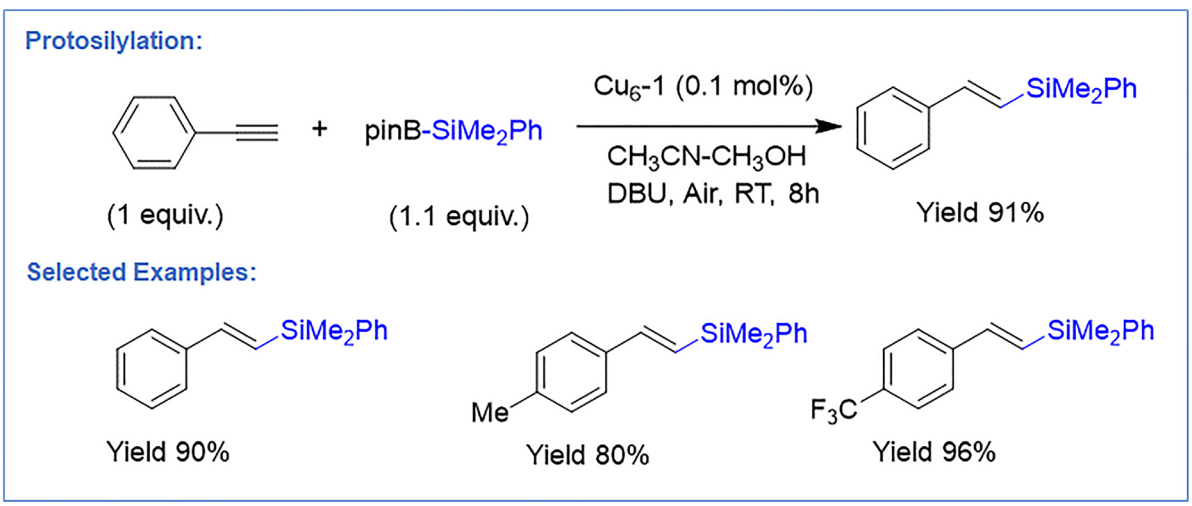

Fig. 11 Representation of protosilylation reaction by Cu_6-1 NCs with substrate scope and corresponding yields.

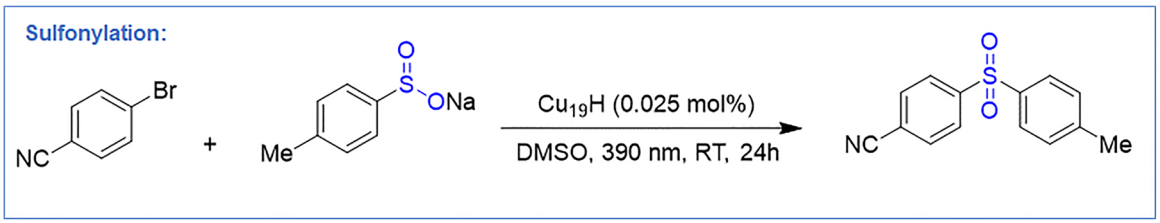

Fig. 12 Representation of sulfonylation reaction with $Cu_{19}H$ NC.

heterogeneous catalysis with full recyclability over five cycles. The reaction showed broad scope: aryl bromides bearing electron-donating, electron-withdrawing, steric, or heteroaryl substituents (–CN, –OMe, –^{t}Bu, –F, –COPh, –CF_3; pyridyl, quinolinyl, thiophenyl) afforded sulfones in 61–88% yield. Various sodium sulfinates (aryl and alkyl) also coupled efficiently (68–86% yield). Late-stage sulfonylation of drug-derived molecules proceeded in 71–74% yield, and the TOF was ~400× higher than $[Cu(CH_3CN)_4]BF_4$. Mechanistic experiments (radical clocks, olefin trapping, TEMPO quenching) confirmed a radical pathway. Upon irradiation, $Cu_{19}H$ NC forms a NC–SO_2R species that undergoes SET to the aryl halide, generating an aryl radical and oxidized NC–SO_2R^+. Radical coupling or reductive elimination furnishes the sulfone and regenerates the cluster. DFT calculations supported favorable formation of NC–SO_2R (ΔE = –0.98 eV) and its strong excited-state reducing power (–2.34 V *vs.* Ag/AgCl). This is the sole reported example of a Cu NC serving as a robust, reusable, visible-light-driven photocatalyst for broad C–S bond formation under mild conditions.

3. Conclusion and future outlook

This review summarizes recent advances in Cu NC catalysis for organic transformations, highlighting how the evolution from early, unstable Cu–hydride species to robust, atomically precise, ligand-protected architectures has reshaped Cu catalysis. In contrast to conventional Cu salts and nanoparticles, Cu NCs possess discrete electronic structures, well-defined active sites, and tunable nuclearity, ligand environments, hydride content, and surface accessibility. These features enable direct structure–activity correlations and provide mechanistic insight that is largely inaccessible in traditional catalytic systems.

Cu NCs display exceptional versatility across a broad range of reactions, including cycloadditions, C–C and C–N couplings, hydroboration, hydrogenation, oxidation, protosilylation, sulfonylation, and multicomponent transformations. Their catalytic performance is governed not merely by Cu identity but by subtle structural factors such as single-atom vacancies, ligand dynamics, mixed-valence states, hydride distribution, and exposed metal sites. Small structural variations can dramatically alter reaction pathways, switching between radical and polar mechanisms, modulating selectivity, and enhancing catalytic efficiency. Collectively, these studies establish Cu NCs as molecularly defined catalysts that bridge homogeneous, heterogeneous, and photocatalytic regimes.

Looking ahead, several directions are expected to drive further progress. Atomically precise bimetallic and multimetallic NCs offer opportunities to exploit synergistic effects and unlock new reactivity through controlled heterometal incorporation. Defect and vacancy engineering will continue to emerge as a powerful tool for tuning electronic structure and generating highly active catalytic sites. Advances in dynamic and adaptive ligand design are likely to enable stimulus-responsive catalysis and enzyme-like flexibility. Deeper understanding of hydride chemistry will expand Cu NC applications in selective hydrogenation and hydrogen-transfer processes, while integration of photocatalytic and electrocatalytic platforms may enable efficient solar- and electricity-driven transformations. Finally, addressing challenges related to stability, scalability, and catalyst recyclability will be essential for translating Cu NCs into practical and sustainable catalytic systems. Overall, Cu NCs represent a unique and rapidly advancing class of catalysts in which atomic precision enables rational design, mechanistic clarity, and exceptional performance. Given the central importance of organocatalytic transformations in modern synthetic chemistry, continued efforts toward developing well-defined catalytic systems are essential for achieving deeper mechanistic insight and improved control over catalytic activity and selectivity. Continued synergy between synthesis, advanced characterization, and theory will be critical for realizing their full potential in organic synthesis and beyond.

Conflicts of interest

There are no conflicts to declare.

Data availability

No primary research results, software or code have been included and no new data were generated or analysed as part of this review.

Acknowledgements

This work was supported by the Japan Society for the Promotion of Science (JSPS) KAKENHI (grant no. 23H00289 and 22K19012), Scientific Research on Innovative Areas ''Aquatic Functional Materials'' (grant no. 22H04562), the Yazaki Memorial Foundation for Science and Technology, and the

Ogasawara Foundation for the Promotion of Science and Engineering.

References

1 R. Jin, C. Zeng, M. Zhou and Y. Chen, *Chem. Rev.*, 2016, **116**, 10346–10413.
2 I. Chakraborty and T. Pradeep, *Chem. Rev.*, 2017, **117**, 8208–8271.
3 H. Hirai, S. Ito, S. Takano, K. Koyasu and T. Tsukuda, *Chem. Sci.*, 2020, **11**, 12233–12248.
4 Y. Du, H. Sheng, D. Astruc and M. Zhu, *Chem. Rev.*, 2019, **120**, 526–622.
5 Z. Hens and J. De Roo, *J. Am. Chem. Soc.*, 2020, **142**, 15627–15637.
6 R. Jin, *Nanoscale*, 2015, **7**, 1549–1565.
7 H. Qian, M. Zhu, Z. Wu and R. Jin, *Acc. Chem. Res.*, 2012, **45**, 1470–1479.
8 R. Jin, Y. Charles Cao, E. Hao, G. S. Métraux, G. C. Schatz and C. A. Mirkin, *Nature*, 2003, **425**, 487–490.
9 X. Kang and M. Zhu, *Chem. Soc. Rev.*, 2019, **48**, 2422–2457.
10 Y.-Z. Huang, R. K. Gupta, G.-G. Luo, Q.-C. Zhang and D. Sun, *Coord. Chem. Rev.*, 2024, **499**, 215508.
11 Y. Lu and W. Chen, *Chem. Soc. Rev.*, 2012, **41**, 3594–3623.
12 H. Yu, B. Rao, W. Jiang, S. Yang and M. Zhu, *Coord. Chem. Rev.*, 2019, **378**, 595–617.
13 Z.-Y. Liu, Q.-B. Nie, B.-L. Han, R. K. Gupta, G.-L. Dong, G.-G. Luo, Z.-L. Yang and D. Sun, *Chem. Soc. Rev.*, 2025, **54**, 9092–9115.
14 Y. Jin, C. Zhang, X.-Y. Dong, S.-Q. Zang and T. C. Mak, *Chem. Soc. Rev.*, 2021, **50**, 2297–2319.
15 S. Biswas, S. Das and Y. Negishi, *Coord. Chem. Rev.*, 2023, **492**, 215255.
16 R. K. Gupta, Z. Wang, B. Mohan, C. H. Tung and D. Sun, *Adv. Mater.*, 2024, **36**, 2410054.
17 Y. Li, M. Zhou and R. Jin, *Adv. Mater.*, 2021, **33**, 2006591.
18 A. W. Cook and T. W. Hayton, *Acc. Chem. Res.*, 2018, **51**, 2456–2464.
19 Z. J. Guan, J. J. Li, F. Hu and Q. M. Wang, *Angew. Chem., Int. Ed.*, 2022, **61**, e202209725.
20 Q. Tang, G. Hu, V. Fung and D.-E. Jiang, *Acc. Chem. Res.*, 2018, **51**, 2793–2802.
21 Z. Lei, X.-K. Wan, S.-F. Yuan, Z.-J. Guan and Q.-M. Wang, *Acc. Chem. Res.*, 2018, **51**, 2465–2474.
22 S. Biswas, A. K. Das and S. Mandal, *Acc. Chem. Res.*, 2023, **56**, 1838–1849.
23 B. Zhang, J. Chen, Y. Cao, O. J. H. Chai and J. Xie, *Small*, 2021, **17**, 2004381.
24 J. Yan, B. K. Teo and N. Zheng, *Acc. Chem. Res.*, 2018, **51**, 3084–3093.
25 T. Higaki, Q. Li, M. Zhou, S. Zhao, Y. Li, S. Li and R. Jin, *Acc. Chem. Res.*, 2018, **51**, 2764–2773.
26 Z. Lei, X.-K. Wan, S.-F. Yuan, J.-Q. Wang and Q.-M. Wang, *Dalton Trans.*, 2017, **46**, 3427–3434.
27 Q. Yao, T. Chen, X. Yuan and J. Xie, *Acc. Chem. Res.*, 2018, **51**, 1338–1348.
28 Y.-P. Xie, J.-L. Jin, G.-X. Duan, X. Lu and T. C. Mak, *Coord. Chem. Rev.*, 2017, **331**, 54–72.
29 Q. Yao, M. Zhu, Z. Yang, X. Song, X. Yuan, Z. Zhang, W. Hu and J. Xie, *Nat. Rev. Mater.*, 2025, **10**, 89–108.
30 S. Maity, S. Kolay, S. Chakraborty, A. Devi and A. Patra, *Chem. Soc. Rev.*, 2025, **54**, 1785–1844.
31 J.-H. Huang, Y. Cui, Z.-Y. Wang and S.-Q. Zang, *Acc. Chem. Res.*, 2025, **58**, 1249–1261.
32 J. Qian, Z. Yang, J. Lyu, Q. Yao and J. Xie, *Precision Chem.*, 2024, **2**, 495–517.
33 Z. Yang, Y. Wang, R. Zhang, T. Chen and J. Xie, *Adv. Mater.*, 2025, e08578.
34 S. Biswas, Y. Shingyouchi, M. Ogami, M. Kamiyama, T. Kawawaki and Y. Negishi, *EcoEnergy*, 2024, **2**, 400–418.
35 Z.-H. Zheng, F.-X. Xiao and Y.-J. Xu, *Small*, 2025, **21**, 2505282.
36 X. Du and R. Jin, *ACS Nano*, 2019, **13**, 7383–7387.
37 S. Rodríguez-Nuévalos, M. Espinosa and A. Leyva-Pérez, *Commun. Chem.*, 2024, **7**, 76.
38 X. Pan, Y. Yao, M. Zhang, X. Yuan, Q. Yao and W. Hu, *Nanoscale*, 2024, **16**, 8196–8215.
39 J. Q. Fan, J. X. Guo and M. B. Li, *Chem. – Eur. J.*, 2025, e02620.
40 D. Yang, J. Wang, Q. Wang, Z. Yuan, Y. Dai, C. Zhou, X. Wan, Q. Zhang and Y. Yang, *ACS Nano*, 2022, **16**, 15681–15704.
41 P. Kumar and M. Nemiwal, *Chem. Asia. J.*, 2024, **19**, e202400062.
42 R. K. Gupta, Z. Wang, B. Mohan, C. H. Tung and D. Sun, *Adv. Funct. Mater.*, 2025, 2507047.
43 X. Liu and D. Astruc, *Coord. Chem. Rev.*, 2018, **359**, 112–126.
44 M. Kamiyama, Y. Shingyouchi, R. Sarma, M. Ghosh, T. Kawawaki, S. Biswas and Y. Negishi, *Chem. Commun.*, 2025, **61**, 1048–1062.
45 A. Baghdasaryan and T. Bürgi, *Nanoscale*, 2021, **13**, 6283–6340.
46 M. Chen, C. Guo, L. Qin, L. Wang, L. Qiao, K. Chi and Z. Tang, *Nano-Micro Lett.*, 2025, **17**, 83.
47 A. K. Das, S. Biswas, V. S. Wani, A. S. Nair, B. Pathak and S. Mandal, *Chem. Sci.*, 2022, **13**, 7616–7625.
48 A. K. Das, S. Hegde, T. J. Woods, V. S. Wani and M. P. Backlund, *Nano Lett.*, 2025, **25**, 7491–7498.
49 A. Jana, S. Duary, A. Das, A. R. Kini, S. Acharya, J. Machacek, B. Pathak, T. Base and T. Pradeep, *Chem. Sci.*, 2024, **15**, 13741–13752.
50 A. Patra, K. Shinde, S. Mandal, A. Kudlu, W.-D. Si, M. Francis, A. Das, D. Sun and S. Roy, *Inorg. Chem.*, 2025, **64**, 20666–20678.
51 B. L. Han, F. Alkan, Z. R. Yuan, P. Mahato, Z. Wang, C. H. Tung and D. Sun, *Angew. Chem., Int. Ed.*, 2025, **64**, e202507412.
52 H. Zhao, C. Zhang, B.-L. Han, P. Mahato, C.-Z. Yang, P.-X. Yu, Z. Wang, C.-H. Tung and D. Sun, *Nano Lett.*, 2025, **25**, 9132–9138.
53 S. Biswas, S. Das and Y. Negishi, *Nanoscale Horiz.*, 2023, **8**, 1509–1522.
54 S. Biswas, Y. Shingyouchi, M. Kamiyama, M. K. Jena, M. Ogami, T. Kawawaki, B. Pathak and Y. Negishi, *Small*, 2025, **21**, 2500302.
55 S. Biswas, T. Tanaka, H. Song, M. Ogami, Y. Shingyouchi, S. Hossian, M. Kamiyama, T. Kosaka, R. Nakatani, Y. Niihori, S. Das, T. Kawawaki, D.-E. Jiang and Y. Negishi, *Small Sci.*, 2025, **5**, 2400465.
56 S. Biswas, Y. Shingyouchi, M. Kamiyama, M. Ogami, H. Song, B. Li, S. Wang, T. Kawawaki, D.-E. Jiang and Y. Negishi, *J. Am. Chem. Soc.*, 2025, **147**, 23733–23742.
57 Y. Shingyouchi, M. Ogami, S. Biswas, T. Tanaka, M. Kamiyama, K. Ikeda, S. Hossain, Y. Yoshigoe, D. Osborn and G. F. Metha, *Small*, 2025, **21**, 2409910.
58 J. Oliver-Messeguer, L. Liu, S. García-García, C. Canós-Giménez, I. Domínguez, R. Gavara, A. Doménech-Carbó, P. Concepción, A. Leyva-Pérez and A. Corma, *J. Am. Chem. Soc.*, 2015, **137**, 3894–3900.
59 R. Greco, E. Tiburcio, B. Palomar-De Lucas, J. Ferrando-Soria, D. Armentano, E. Pardo and A. Leyva-Pérez, *Mol. Catal.*, 2022, **522**, 112228.
60 A. Pal, S. Biswas, B. Sahoo and Y. Negishi, *Synlett*, 2025, 1123–1129.
61 A. Sagadevan, K. Murugesan, O. M. Bakr and M. Rueping, *Chem. Commun.*, 2024, **60**, 13858–13866.
62 R. S. Dhayal, W. E. van Zyl and C. W. Liu, *Acc. Chem. Res.*, 2016, **49**, 86–95.
63 P.-K. Liao, C.-S. Fang, A. J. Edwards, S. Kahlal, J.-Y. Saillard and C. W. Liu, *Inorg. Chem.*, 2012, **51**, 6577–6591.
64 R. S. Dhayal, J.-H. Liao, Y.-R. Lin, P.-K. Liao, S. Kahlal, J.-Y. Saillard and C. W. Liu, *J. Am. Chem. Soc.*, 2013, **135**, 4704–4707.
65 J.-H. Liao, R. S. Dhayal, X. Wang, S. Kahlal, J.-Y. Saillard and C. W. Liu, *Inorg. Chem.*, 2014, **53**, 11140–11145.
66 A. J. Edwards, R. S. Dhayal, P. K. Liao, J. H. Liao, M. H. Chiang, R. O. Piltz, S. Kahlal, J. Y. Saillard and C. W. Liu, *Angew. Chem., Int. Ed.*, 2014, **53**, 7214–7218.
67 R. S. Dhayal, J. H. Liao, X. Wang, Y. C. Liu, M. H. Chiang, S. Kahlal, J. Y. Saillard and C. W. Liu, *Angew. Chem., Int. Ed.*, 2015, **54**, 13604–13608.
68 S. Biswas and Y. Negishi, *Dalton Trans.*, 2024, **53**, 9657–9663.
69 S. Biswas and Y. Negishi, *J. Phys. Chem. Lett.*, 2024, **15**, 947–958.
70 X. Ge, S. Zeng, H. Deng, B. K. Teo and C. Sun, *Coord. Chem. Rev.*, 2024, **503**, 215667.
71 M. Ghosh, R. Sarma, M. Kamiyama, T. Kawawaki, S. Biswas and Y. Negishi, *Nanoscale Horiz.*, 2025, **10**, 1250–1267.
72 W. S. Mahoney, D. M. Brestensky and J. M. Stryker, *J. Am. Chem. Soc.*, 1988, **110**, 291–293.
73 B. H. Lipshutz and B. A. Frieman, *Synfacts*, 2006, 0047.
74 C. Deutsch, N. Krause and B. H. Lipshutz, *Chem. Rev.*, 2008, **108**, 2916–2927.
75 T. H. Lemmen, K. Folting, J. C. Huffman and K. G. Caulton, *J. Am. Chem. Soc.*, 1985, **107**, 7774–7775.

76 A. W. Cook, Z. R. Jones, G. Wu, S. L. Scott and T. W. Hayton, *J. Am. Chem. Soc.*, 2018, **140**, 394–400.
77 G. Yang, Y. Xie, Y. Wang, Y. Tang, L. L. Chng, F. Jiang, F. Du, X. Zhou, J. Y. Ying and X. Yuan, *Nano Res.*, 2023, **16**, 1748–1754.
78 H. Zhou, T. Yang, H. Deng, Y. Yun, S. Jin, L. Xiong and M. Zhu, *Nanoscale*, 2024, **16**, 10318–10324.
79 Y.-Q. Xiao, P. Shang, X.-Y. Chen, X.-Q. Pu, K.-W. Jiang and X.-F. Jiang, *Chem. Mater.*, 2024, **36**, 2027–2038.
80 C. Dong, R. W. Huang, A. Sagadevan, P. Yuan, L. Gutiérrez-Arzaluz, A. Ghosh, S. Nematulloev, B. Alamer, O. F. Mohammed, I. Hussain, M. Rueping and O. M. Bakr, *Angew. Chem., Int. Ed.*, 2023, **62**, e202307140.
81 T. Jia, Y.-X. Li, X.-H. Ma, M.-M. Zhang, X.-Y. Dong, J. Ai and S.-Q. Zang, *Nat. Commun.*, 2023, **14**, 6877.
82 L.-J. Liu, M.-M. Zhang, Z. Deng, L.-L. Yan, Y. Lin, D. L. Phillips, V. W.-W. Yam and J. He, *Nat. Commun.*, 2024, **15**, 4688.
83 S. Nematulloev, A. Sagadevan, B. Alamer, A. Shkurenko, R. Huang, J. Yin, C. Dong, P. Yuan, K. E. Yorov, A. A. Karluk, W. J. Mir, B. E. Hasanov, M. N. Hedhili, N. M. Halappa, M. Eddaodi, O. F. Mohammed, M. Rueping and O. M. Bakr, *Angew. Chem., Int. Ed.*, 2023, **62**, e202303572.
84 S. Biswas, A. Pal, M. K. Jena, S. Hossain, J. Sakai, S. Das, B. Sahoo, B. Pathak and Y. Negishi, *J. Am. Chem. Soc.*, 2024, **146**, 20937–20944.
85 S. Lee, M. S. Bootharaju, G. Deng, S. Malola, W. Baek, H. Hakkinen, N. Zheng and T. Hyeon, *J. Am. Chem. Soc.*, 2020, **142**, 13974–13981.
86 A. K. Das, S. Biswas, A. Pal, S. S. Manna, A. Sardar, P. K. Mondal, B. Sahoo, B. Pathak and S. Mandal, *Nanoscale*, 2024, **16**, 3583–3590.
87 A. Sagadevan, A. Ghosh, P. Maity, O. F. Mohammed, O. M. Bakr and M. Rueping, *J. Am. Chem. Soc.*, 2022, **144**, 12052–12061.
88 B. Mondal, K. Basu, R. Jana, P. Mondal, B. Hansda, A. Datta and A. Banerjee, *ACS Appl. Nano Mater.*, 2022, **5**, 7932–7943.
89 B. Alamer, A. Sagadevan, M. Bodiuzzaman, K. Murugesan, S. Alsharif, R.-W. Huang, A. Ghosh, M. H. Naveen, C. Dong, S. Nematulloev, J. Yin, A. Shkurenko, M. Abulikemu, X. Dong, Y. Han, M. Eddaudi, M. Rueping and O. M. Bakr, *J. Am. Chem. Soc.*, 2024, **146**, 16295–16305.
90 T. Jia, J. Ai, X. Li, M.-M. Zhang, Y. Hua, Y.-X. Li, C.-F. Sun, F. Liu, R.-W. Huang, Z. Wang and S.-Q. Zang, *Nat. Commun.*, 2024, **15**, 9551.
91 C. Sun, N. Mammen, S. Kaappa, P. Yuan, G. Deng, C. Zhao, J. Yan, S. Malola, K. Honkala, H. Häkkinen, B. K. Teo and N. Zheng, *ACS Nano*, 2019, **13**, 5975–5986.
92 F. Lan, J. Aarons, Y. Shu, X. Zhou, H. Jiao, H. Wang, Q. Guan and W. Li, *Appl. Catal., B*, 2021, **299**, 120651.
93 G. Dong, Z. Pan, B. Han, Y. Tao, X. Chen, G.-G. Luo, P. Sun, C. Sun and D. Sun, *Angew. Chem., Int. Ed.*, 2023, **62**, e202302595.
94 G.-G. Luo, Z.-H. Pan, B.-L. Han, G.-L. Dong, C.-L. Deng, M. Azam, Y.-W. Tao, J. He, C.-F. Sun and D. Sun, *Angew. Chem., Int. Ed.*, 2023, **62**, e202306849.
95 C.-Y. Liu, T.-Y. Liu, Z.-J. Guan, S. Wang, Y.-Y. Dong, F. Hu, D.-E. Jiang and Q.-M. Wang, *CCS Chem.*, 2024, **6**, 1581–1590.
96 K. Basu, S. Paul, R. Jana, A. Datta and A. Banerjee, *ACS Sustainable Chem. Eng.*, 2019, **7**, 1998–2007.
97 S. Li, Q. Wu, X. You, X. Ren, P. Du, F. Li, N. Zheng and H. Shen, *J. Am. Chem. Soc.*, 2024, **146**, 27852–27860.
98 Y.-M. Wang, X.-C. Lin, K.-M. Mo, M. Xie, Y.-L. Huang, G.-H. Ning and D. Li, *Angew. Chem., Int. Ed.*, 2023, **62**, e202218369.
99 M. Bodiuzzaman, K. Murugesan, P. Yuan, B. Maity, A. Sagadevan, N. Malenahalli H, S. Wang, P. Maity, M. F. Alotaibi, D. E. Jiang, M. Abulikemu, O. F. Mohammed, L. Cavallo, M. Rueping and O. M. Bakr, *J. Am. Chem. Soc.*, 2024, **146**, 26994–27005.
100 C. Zhang, Z. Wang, W. D. Si, L. Wang, J. M. Dou, Z. Y. Gao, C. H. Tung and D. Sun, *ACS Nano*, 2022, **16**, 9598–9607.
101 L.-J. Liu, J.-W. Zhang, M. Asad, Z.-Y. Wang, S.-Q. Zang and T. C. Mak, *Chem. Commun.*, 2021, **57**, 5586–5589.
102 S. Wen, C. Zhang, L. J. Liu, Z. Wang, D. Sun and J. He, *Angew. Chem., Int. Ed.*, 2025, **64**, e202416851.
103 M. F. Alotaibi, A. Sagadevan, P. Yuan, M. Bodiuzzaman, K. Murugesan, R. Zhou, J. Yin, S. Thomas, R. W. Huang, N. M. Halappa, C. Dong, M. Abulikemu, H. N. Alshareef, O. F. Mohammed, M. Rueping and O. M. Bakr, *J. Am. Chem. Soc.*, 2025, **147**, 28932–28942.

